LRRK2 mutations block NCOA4 trafficking upon iron overload leading to ferroptotic death

Andres Goldman[1, 5] 0000-0002-0322-139X, Mai Nguyen[1, 5], Joel Lanoix[2, 5] 0000-0001-7073-9298, Chongyang Li[2] 0000-0001-6842-4406, Ahmed Fahmy[3, 5] 0000-0003-0444-383X, Yong Zhong Xu[4,5]0000-0002-9201-0446, Erwin Schurr[4, 5] 0000-0002-2640-536X, Pierre Thibault[2, 5] 0000-0001-5993-0331, Michel Desjardins[3, 5] 0000-0002-5684-5980, and Heidi M. McBride[1, 5,*] 0000-0003-4666-2280

[1]Montreal Neurological Institute, McGill University 3801 University Ave, Montreal, Quebec
[2]Institute for Research in Immunology and Cancer (IRIC), Université de Montréal, Montréal, Québec, Canada; Department of Chemistry, Université de Montréal, Montréal, Québec, Canada.
[3]Département de pathologie et biologie cellulaire, Université de Montréal, Montréal, Québec, Canada
[4]Program in Infectious Diseases and Immunity in Global Health, The Research Institute of the McGill University Health Centre; Montreal, QC, Canada and Departments of Human Genetics and Medicine, Faculty of Medicine and Health Science, McGill University, Montreal, Quebec, Canada
5 Aligning Science Across Parkinson's (ASAP) Collaborative Research Network, Chevy Chase, MD 20815, USA

*to whom correspondence be addressed.

Abstract:

Altered iron homeostasis has long been implicated in Parkinson's Disease (PD), although the mechanisms have not been clear. Given the critical role of PD-related activating mutations in LRRK2 (leucine-rich repeat protein kinase 2) within membrane trafficking pathways we examined the impact of a homozygous mutant LRRK2G2019S on iron homeostasis within the RAW macrophage cell line with high iron capacity. Proteomics analysis revealed a dysregulation of iron-related proteins in steady state with highly elevated levels of ferritin light chain and a reduction of ferritin heavy chain. LRRK2G2019S mutant cells showed efficient ferritinophagy upon iron chelation, but upon iron overload there was a near complete block in the degradation of the ferritinophagy adaptor NCOA4. These conditions lead to an accumulation of phosphorylated Rab8 at the plasma membrane, which is selectively inhibited by LRRK type II kinase inhibitors. Iron overload then leads to increased oxidative stress and ferroptotic cell death. These data implicate LRRK2 as a key regulator of iron homeostasis and point to the need for an increased focus on the mechanisms of iron dysregulation in PD.

Introduction:

Age-related neurodegenerative diseases are an increasing burden on the global population. Detailing the precise mechanisms responsible pathology in these complex diseases has been challenging. Hallmark features of Parkinson's Disease (PD) are motor symptoms, namely tremor and rigidity, and selective death of neuromelanin-containing dopamine neurons in the *substantia nigra pars compacta* (SNpc) and *locus coeruleus*. About 5-15% of PD is familial

and current estimates recognize over 50 causal variants and 100 risk alleles (Lim et al., 2024). These highlight contributions of mitochondria and lysosomal function, the spreading of prion-like synuclein filaments, innate and adaptive immune pathways, and more (Cannon and Gruenheid, 2022; Johnson et al., 2019; Tansey et al., 2022). In the remaining ~90% of sporadic PD, it is unclear what the underlying causes may be, although environmental factors like heavy metals or pesticides (Aravindan et al., 2024), and various types of infection (Cannon and Gruenheid, 2022) are under intense investigation.

An early candidate cause of selective vulnerability of dopamine neurons in PD was their high dependence on iron metabolism required for synthesis of dopamine and production of neuromelanin, which captures and stores excess iron (Jenner, 1989; Sulzer et al., 2000). PD patients show dramatic losses of pigmented neuromelanin, which is a hallmark feature in autopsied brain. The loss of neuromelanin results in higher levels of free iron, which is being explored as a biomarker in early-stage PD patients by high-resolution MRI quantitative susceptibility mapping (Guan et al., 2024). The mechanisms by which iron may be mishandled in the SNpc are understudied, and causality to PD pathology is not clearly established. However, there is increasing speculation that in PD increased iron toxicity may cause ferroptotic cell death, making iron the Achilles' heel of dopaminergic neurons (Jenner, 1989; Masaldan et al., 2019; Riederer et al., 2023). To test these ideas clinically, a series of trials were initiated employing iron chelators in PD patients, with mixed results (Devos et al., 2025). New formulations and approaches are still under investigation, highlighting the importance of a better understanding of the impact of iron on PD pathology.

A common risk factor for inherited PD are variants in the *LRRK2* gene which encodes a large kinase with a complex array of domains including armadillo repeat, ankyrin, WD40, ROC-COR (Ras of complex proteins [ROC] and C-terminal of ROC [COR]) GTPase domains, leucine-rich repeat, and a kinase domain (Alessi and Pfeffer, 2024). The penetrance of PD in carriers of LRRK2 pathogenic variants is typically ~50% at age 70, rising to 75% at 80 years, implicating additional genetic and / or environmental factors in disease progression (Mata et al., 2023). LRRK2 variants have been the subject of intense research efforts which have demonstrated an involvement in cellular functions that range from subcellular protein trafficking (Singh and Muqit, 2020), lysosomal repair/function (Bentley-DeSousa et al., 2025), cytoskeletal dynamics (Leschziner and Reck-Peterson, 2021), ciliogenesis and centrosome cohesion (Jaimon et al., 2025; Li et al., 2024; Lin et al., 2025; Madero-Perez et al., 2018), mitochondrial function (Buck and Sanders, 2025), synaptic transmission (Kuhlmann & Milnerwood 2020), and immune responses (Peter and Strober, 2023). Despite much progress, the molecular basis of LRRK2 pathogenicity remains unclear.

All pathogenic LRRK2 variants, within and outside of LRRK2's kinase domain, increase its serine-threonine kinase activity, including the most common pathogenic substitution p.G2019S ($LRRK2_{G2019S}$) (Mata et al., 2023). In addition to autophosphorylation, LRRK2 substrates include numerous Rab GTPases that regulate vesicular transport; these are hyperphosphorylated in cells from LRRK2 PD patients and models (Alessi and Pfeffer, 2024; Steger et al., 2016). The downstream impact of each phosphorylated Rab on membrane transport and signaling pathways appears highly dependent on the cell type and context, and the field has not reached consensus on which of the many implicated LRRK2 variant phenotypes are the driver of disease. However, Rab hyperphosphorylation is observed in other genetic forms of PD (e,g., VPS35 (Kadgien et al., 2021; Mir et al., 2018), and idiopathic PD brains (Di Maio et al.,

2018). Thus, there is a breadth of evidence associating LRRK2 kinase *gain-of-function* with PD pathogenesis.

In the context of iron handling, previous work reported context-specific changes in iron homeostasis in cells carrying the $LRRK2_{G2019S}$ mutation in HEK293T cells and iPSC-derived microglia (Mamais et al., 2025; Mamais et al., 2021). It was initially shown that the phosphorylation of Rab8, a key LRRK2 substrate, reduced its interaction with its GTP exchange factor Rabin8, which in turn led to the lysosomal degradation of the transferrin receptor. They observed the accumulation of ferritin and free iron in microglia of $LRRK2_{G2019S}$ mice following injections with LPS, although the mechanisms underlying these changes *in vivo* were not established (Mamais et al., 2021). While iron phenotypes have not been observed consistently within $LRRK2_{G2019S}$ mutant cells, single-cell RNA sequencing experiments did report a cell-specific loss in ferritin heavy chain mRNA within $LRRK2_{G2019S}$ mice, specifically in astrocytes, microglia, and oligodendrocytes (Khan et al., 2024).

Given evidence supporting a contributing role of dysregulated iron homeostasis in PD, we explored the impact of LRRK2 mutations on iron transport and handling in a cultured macrophage model. The data provide evidence that RAW macrophages carrying the $LRRK2_{G2019S}$ mutation have altered iron homeostasis in steady state conditions, which lead to an inability to handle iron overload resulting in oxidative stress and ferroptotic cell death. We observed a block in the normal iron-induced expansion of lysosomes and in the microautophagy driven degradation of the ferritin autophagy receptor NCOA4. Interestingly, iron overload conditions in $LRRK2_{G2019S}$ cells leads to high levels of of the LRRK2 substrate p-Rab8 accumulating on the plasma membrane. This phosphorylation is resistant to the type I LRRK2 kinase inhibitor MLi-2, but remains sensitive to both the pan-specific type II kinase inhibitor rebastinib and the newly developed LRRK selective type II kinase inhibitors RN277 and RN341 (Raig et al., 2025). Iron overload conditions are not common in healthy physiology but are a significant factor in PD brains. Should this aspect of LRRK2 mutant function be relevant to the death of dopaminergic neurons, our results would suggest the use of MLi-2 may not be effective in this context, where LRRK2 selective type II kinase inhibitors would be active in iron related pathologies linked to LRRK2.

Results:

$LRRK2_{G2019S}$ RAW macrophages have altered iron homeostasis

Macrophages ingest aged red blood cells and have a unique capacity to handle high levels of iron (Winn et al., 2020). Therefore, we considered macrophages, given the high levels of LRRK2 expression (Gardet et al., 2010), as a good model system to interrogate the impact of pathogenic homozygous LRRK2 mutations on iron handling. To this end we generated a CRISPR-knock-in RAW264.7 macrophage cell line carrying the $LRRK2_{G2019S}$ mutation (**Supplemental Fig 1A**). To confirm the increased in LRRK2 kinase activity in this line we probed cell extracts with two phospho-specific antibodies (**Figure 1A**). LRRK2 autophosphorylation was increased, as seen with an antibody recognizing $LRRK2_{pS1292}$. A second antibody recognizing phosphorylated $Rab8_{T72}$ (with some lower specificity for p-Rab10 and p-Rab35) (Lis et al., 2018), further confirmed an increased kinase activity in the CRISPR-edited $LRRK2_{G2019S}$ macrophages, with no change in total Rab8 levels across the genotypes (**Fig1A**). Both phosphorylation events were reversed upon treatment with the type I LRRK2 kinase inhibitor MLi-2 (**Figure 1A, quantification in 1B**). These data confirm the successful generation of the *gain-of-function* variant. We then performed unbiased whole cell proteomics

137 and found significant changes in many proteins important for iron homeostasis (**Figure 1C,D)**.
138 Protein quantification by western blot validated downregulation of the transferrin receptor (TfR)
139 responsible for iron uptake, downregulation of the ferritin heavy chain (FTH), and upregulation
140 of ferritin light chain (FTL), both critical for iron storage (**Figure 1E, quantified in Supp**
141 **Figure 1B**). Iron is found inside the cell in its reactive ferrous (Fe^{2+}) or mineralized ferric (Fe^{3+})
142 state. Fe^{2+} is the form required by the cell to forge iron sulfur clusters and heme groups, while
143 excess free ferrous iron can catalyze the generation of free radical species through the Fenton
144 reaction (Galy et al., 2024). This makes Fe^{2+} essential, yet potentially toxic, for the cell. Excess
145 Fe^{2+} is rapidly captured by cytosolic ferritin where iron is harmlessly stored in the mineralized
146 ferric Fe^{3+} state (Chasteen and Harrison, 1999; Melman and Bou-Abdallah, 2020). FTH and FTL
147 together form cage-like complexes that can hold up to ~4500 atoms of Fe^{3+}. FTH has enzymatic
148 ferroxidase activity required to oxidize Fe^{2+} into Fe^{3+} for safe storage (Melman and Bou-
149 Abdallah, 2020). We quantified the iron content and composition and found that $LRRK2_{G2019S}$
150 macrophages have reduced total iron content, marked by a selective loss of mineralized iron
151 Fe^{3+}, and 2-fold increase in Fe^{2+} content, compared to WT control (**Figure 1 F).** This result was
152 validated using the fluorescent FerroOrange probe, which reported a similar 2-fold increase of
153 labile Fe^{2+} in $LRRK2_{G2019S}$ macrophages (Niwa et al., 2014) (**Supp Figure 1C,D**).
154 The iron quantification revealed a cellular reduction in total iron, yet we observed excess
155 FTL and reduced TfR which canonically suggests a translational response to iron overload
156 through the iron-response elements (IRE) within their mRNA (Galy et al., 2024; Rouault, 2006).
157 We therefore tested a series of additional iron-related proteins regulated by either the iron-sulfur
158 cluster binding iron responsive protein 1 (IRP1), or the Fe2+ regulated iron response protein 2
159 (IRP2). $LRRK2_{G2019S}$ expression did not elicit any changes in the levels of HERC2/FBXL5/IRP2
160 axis (**Supp Figure 1E**), indicating IRP2 is not activated. In addition, we found the levels of other
161 proteins harboring IREs such as DMT1 or ferroportin were unaffected in $LRRK2_{G2019S}$
162 macrophages (**Supp Figure 1E**), implying the IRP1/2 axis is not involved in the upregulation of
163 FTL or downregulation of TfR. This indicates that the changes in FTL and FTH levels are not
164 through canonical iron response element mechanisms.
165 We further tested the enzymatic activity of the iron-sulfur containing IRP1 (also called
166 Aconitase 1 or ACO1) which is often used as a proxy to monitor any deficits in iron-sulfur
167 cluster assemblies (Beinert and Kennedy, 1993). As expected, given the evidence that the
168 translational regulation by IRP1 was unaltered, $LRRK2_{G2019S}$ macrophages did not show any
169 change in ACO1 activity **(Supp Figure 1F**). This further indicates that the delivery of ferrous
170 Fe^{2+} iron to mitochondria for the biogenesis of iron-sulfur complexes remained intact. Therefore,
171 $LRRK2_{G2019S}$ leads to a significant reduction in total cellular iron (**Figure 1F**), primarily due to
172 the loss of stored ferric Fe^{3+}, and an increase in ferrous Fe^{2+}, without an impairment of functional
173 delivery of $Fe^{2+}$to mitochondria or the modulation of iron related protein synthesis pathways
174 (**Supp Figs. 1E,F**).
175 FTH is critical for the lysosomal degradation of ferritin complexes through an autophagic
176 process termed ferritinophagy (Dowdle et al., 2014; Kuno et al., 2022; Mancias et al., 2015;
177 Mancias et al., 2014; Ohshima et al., 2022; Zhao et al., 2024). Given the absence of FTH
178 expression, we considered this could cause a block in complex turnover, resulting in the
179 observed increases in FTL levels. To monitor the turnover of FTL we generated WT and
180 $LRRK2_{G2019S}$ macrophages stably expressing N-terminal cherry tagged FTL to visualize its
181 cellular distribution (Ohshima et al., 2022). In untreated WT cells the cherry-FTL signal is
182 primarily distributed within lysotracker green positive lysosomes, with some cytosolic signal

183 (**Fig 1G, quantified in H**). In contrast, LRRK2$_{G2019S}$ macrophages show a highly diffuse,
184 cytosolic cherry-FTL signal and faint lysosomal localization (**Fig 1G third row**). This
185 observation is consistent with impaired or inefficient lysosomal targeting of FTL in steady state
186 conditions.
187 To determine whether LRRK2$_{G2019S}$ macrophages were capable of induced ferritin
188 degradation, we activated ferritinophagy using the iron chelator desferoxamine (DFO) to remove
189 iron from the cytoplasm (**Figure 1G-I**). Ferritinophagy is regulated by the action of nuclear
190 receptor coactivator 4 (NCOA4), the adaptor protein that binds and delivers ferritin cages into
191 the autophagosome (Dowdle et al., 2014; Kuno et al., 2022; Mancias et al., 2014; Ohshima et al.,
192 2022; Zhao et al., 2024)**.** NCOA4 is an iron and iron sulfur cluster binding protein (Kuno et al.,
193 2022; Zhao et al., 2024). Therefore iron levels modulate NCOA4-ferritin interactions allowing
194 the fine tuning of ferritin turnover where NCOA4 bound to ferritin promotes liquid-liquid phase
195 separated condensates (LLPS) that are selectively degraded through autophagy (Ohshima et al.,
196 2022). Looking first at FTL, DFO treatment increased in the appearance of FTL in lysosomes in
197 WT and LRRK2$_{G2019S}$ macrophages, consistent with functional ferritinophagy (**Figure 1G**
198 **second and fourth rows, quantification in H**). By western blot we confirmed that iron
199 chelation led to increased clearance of FTL in WT and LRRK2$_{G2019S}$ macrophages (**Figure 1I**).
200 With longer exposure the degradative products of FTL were visible in DFO treated LRRK2$_{G2019S}$
201 macrophages (**Figure 1I** black arrow). The ferritinophagy adaptor NCOA4 was also highly
202 elevated in LRRK2 mutant cells at steady state (**Figure 1I**), and we observed that iron chelation
203 led to clearance of NCOA4 in LRRK2$_{G2019S}$ macrophages, consistent with functional
204 ferritinophagy.

205 ### LRRK2$_{G2019S}$ show defects in NCOA4 turnover upon iron overload

206 The inverse of iron chelation is the response to iron overload, which requires NCOA4 to
207 segregate away from ferritin cages, resulting in a diffuse cytosolic distribution of ferritin that
208 stably mineralizes and stores excess iron as Fe^{3+} (Galy et al., 2024). In high iron conditions
209 NCOA4 binds iron sulfur clusters, which promotes binding of the ubiquitin E3 ligase HERC2 to
210 drive NCOA4 degradation through the proteasome (Zhao et al., 2024). In a second degradation
211 pathway, ferric Fe^{3+} bound NCOA4 can drive assembly into phase-condensed foci that become
212 internalized into lysosomes through a microautophagy pathway (Kuno et al., 2022). At later time
213 points of iron overload NCOA4 can also carry low levels of ferritin into the lysosomes through
214 microautophagy to maintain pools of labile iron (Kuno et al., 2022). The precise regulation of
215 these distinct mechanisms remains under intense investigation. In our experiments with ferrous
216 ammonium sulfate (FAS) to induce iron overload, we observe the expected diffuse cytosolic
217 staining of FTL in WT cells (**Supp Figure 2A,B**). In LRRK2$_{G2019S}$ macrophages, FTL is already
218 diffuse in untreated cells, which remains the case upon iron overload, with the addition of a few
219 bright foci resembling phase-condensed foci (**Supp Figure 2A,B**).
220 A critical distinction emerged between the genotypes when imaging cherry-NCOA4. In
221 WT untreated cells cherry-NCOA4 is seen primarily within lysosomes (**Figure 2A**), but in
222 LRRK2$_{G2019S}$ macrophages cherry-NCOA4 had limited lysosomal co-localization and appeared
223 in bright cytosolic foci (**Figure 2A, number and size of foci quantified in 2B,C**). In WT cells
224 treated with FAS NCOA4 appeared in bright cytosolic foci and within lysosomes, which became
225 enlarged (**seen upon FAS treatment in Fig 2A and Supp Figure 2C, quantified in Supp**
226 **2D,E**). In contrast, LRRK2$_{G2019S}$ macrophages showed NCOA4 accumulating in larger bright
227 cytosolic (non-lysosomal) foci, suggesting very little internalization into lysosomes in high iron.

228 Quantification of foci size showed that LRRK2$_{G2019S}$ macrophages had fewer NCOA4 foci with a
229 significant increase in their size relative to WT cells (**Figure 2B,C**).
230 Time-lapse imaging of NCOA4 foci revealed their entry into enlarged lysosomes in FAS
231 treated WT cells (**Figure 2D, Supp Video 1**), as previously described (Ohshima et al., 2022).
232 Conversely, in LRRK2$_{G2019S}$ cells NCOA4 foci did not associate with lysosomes and were thus
233 seemingly unable to undergo microautophagy (**Figure 2D, Supp Video 2**). To biochemically
234 confirm bright cytosolic foci reflected the formation of phase-separated condensates, we
235 examined the amount of NCOA4 within Triton-X insoluble fractionations (Ohshima et al.,
236 2022). Consistently, total insoluble NCOA4 levels were increased in LRRK2$_{G2019S}$ macrophages
237 (**Figure 2E**). Addition of bafilomycin to block degradation in lysosomes led to accumulation of
238 NCOA4 in WT cells in both untreated and iron loaded / FAS conditions (**Figure 2E**). NCOA4
239 also accumulated in bafilomycin exposed LRRK2$_{G2019S}$ cells, however, in bafilomycin the FAS /
240 iron overload failed to increase NCOA4 levels further, indicating a block in lysosomal flux
241 (**Figure 2E**).
242 To examine the expected LRRK2 kinase-dependency of the NCOA4 phenotype, we
243 employed the LRRK2 inhibitor MLi-2 (Fell et al., 2015). MLi-2 reversed the accumulation of
244 NCOA4 in steady-state conditions in both genotypes, indicating that NCOA4 levels are coupled
245 to LRRK2 kinase activity (**Figure 2F**). Upon iron overload in wild type cells we observe an
246 accumulation of NCOA4 that is again reversed upon MLi-2 treatment. Suprisingly, the increased
247 levels of NCOA4 seen in LRRK2$_{G2019S}$ cells was resistant to LRRK2 kinase inhibition, while
248 LRRK2 autophosphorylation was efficiently lost, demonstrating target engagement (**Figure 2F**).
249 Moreover, MLi-2 treatment did not rescue the alterations in ferritin proteins in untreated cells,
250 nor did it rescue the lysosomal morphology linked to iron overload (**Supp Figure 2F-H**). This
251 finding indicates that the block in NCOA4 degradation induced by iron overload within
252 LRRK2$_{G2019S}$ cells is resistant to MLi-2.
253

254 ### LRRK$_{G2019S}$ impact on iron metabolism reveals differential sensitivities to type I and type II kinase
255 inhibitors.

256 Given the unexpected resistance of the NCOA4 phenotypes to MLi-2 in LRRK2$_{G2019S}$
257 cells upon iron overload / FAS conditions (**Figure 2F**), we explored the cellular localization of
258 phosphorylated Rab signal in these conditions. In both wild type and LRRK2$_{G2019S}$ the pRab8
259 was barely detected with immunofluorescence at steady state (**Figure 3A**). Iron overload / FAS
260 did not change this pattern in WT or LRRK2 KO cells. However, in ~30% of LRRK2$_{G2019S}$ cells
261 FAS induced a pronounced upregulation and accumulation of pRab8 signal on plasma membrane
262 ruffles, and coincided with cells showing significant blebbing (**Figure 3A, insets in B,**
263 **quantification in C**). Western blots confirmed the pRab8 signal was specific to LRRK2$_{G2019S}$
264 cells, and enhanced upon iron overload (**Supplemental Figure 3A,B**). To confirm the specificity
265 of the p-Rab8 immunofluorescent signal we validated using siRNA approaches. Silencing Rab8
266 led to a near complete loss of the plasma membrane signal, with partial effect upon silencing
267 Rab10 (**Supp Figure 3C-E**). We further observed p-Rab8 signal consistent with the previously
268 described recruitment of Rab8 to the centrioles in mitotic cells (Madero-Perez et al., 2018)
269 (**Supp Figure 3F**). Lastly, a strong lysosomal p-RAB8 signal using this antibody was seen in
270 cells treated with LLOME, where it has been established that LRRK2-mediated Rab8
271 phosphorylation leads to Rab8 recruitment to damaged lysosomes (**Supp Figure 3G**) (Herbst et
272 al., 2020; Mamais et al., 2021). These data confirm that the pRab8 antibody shows specificity to

273 Rab8 in immunofluorescent experiments showing recruitment to the plasma membrane in iron
274 loaded LRRK2$_{G2019S}$ cells.
275 A similar recruitment of Rab8 to plasma membrane ruffles was previously observed upon
276 activation of Toll-like receptors (Luo et al., 2018; Tong et al., 2021; Wall et al., 2017). There, it
277 was established that TLR-activation of Rab8 recruits its effector PI3Kγ, to generate a signaling
278 platform required to activate AKT/mTOR. We therefore examined AKT phosphorylation at S473
279 as a functional readout of pRab8 recruitment to the cell surface over a time course of FAS
280 treatment. We observed AKT phosphorylation in WT cells, upon FAS / iron overload at 8 hours
281 which was much more pronounced in LRRK2$_{G2019S}$ macrophages (**Supplementary Figure**
282 **3H,quantified in I**). This supports the idea that plasma membrane associated pRab8 is activating
283 established Rab8 function.
284 We next tested whether the pRab8 signal seen upon iron overload in LRRK2$_{G2019S}$ cells
285 was sensitive to MLi-2. As with NCOA4, the pRab8 signal was also resistant to MLi-2 treatment
286 in LRRK2$_{G2019S}$ cells exposed to high iron, while the autophosphorylation of LRRK2 was
287 blocked by the drug (**Figure 3C,D**). Wild type cells show very little pRab8 upon iron loading,
288 which also appears to be insensitive to MLi2, while autophosphorylation of LRRK2 is inhibited
289 (**Figure 3C**). The insensitity to MLi-2 was inconsistent with the overwhelming evidence that the
290 phenotypes of the LRRK2 mutations are due to hyperactivity of the kinase domain. MLi-2 is a
291 type I kinase inhibitor, a class that binds to the active site and stabilizes the active-like, or closed
292 conformation of the kinase. Type II inhibitors, in contrast, stabilize the inactive, open
293 conformation of the kinase. Recent cryo-EM structures of LRRK2 bound to type I and type II
294 inhibitors have highlighted the conformations adopted by LRRK2 when bound to either type of
295 inhibitor (Sanz Murillo et al., 2023; Tasegian et al., 2021; Zhu et al., 2024). We therefore
296 considered whether iron overload may somehow impact the conformation of LRRK2, and tested
297 a broad spectrum type II kinase inhibitor shown previously to efficiently block LRRK2 kinase
298 activity called rebastinib (Tasegian et al., 2021). Unlike MLi-2, treatment of both wild type and
299 LRRK2$_{G2019S}$ cells with rebastinib efficiently blocked the phosphorylation of Rab8 in both the
300 presence or absence of iron overload as seen by western blot (**Figure 3E, quantified in**
301 **Supplemental Figure 3J**), and by immunofluorescence (**Figure 3F, quantified in G**). As
302 rebastinib has broad specificity, with effects on ~30% of the kinome, we turned to the newly
303 developed LRRK-selective type II kinase inhibitors RN277 and RN341 (Raig et al., 2025). As
304 with rebastinib, 8 hour treatment with either of the two new drugs efficiently reversed the plasma
305 membrane pRab8 signal (**Figure 3H, quantified in I**), and as seen by western blot (**Figure**
306 **3J,K**). These data confirm the kinase dependence of Rab8 phosphorylation at the plasma
307 membrane in LRRK2$_{G2019S}$ cells upon treatment with FAS and highlights a cellular condition
308 where we observe differential efficacy between type I and type II LRRK2 kinase inhibitors.
309

310 ### LRRK2$_{G2019S}$ cells are hypersensitive to iron induced oxidation and ferroptotic cell death.

311 In order to interrogate the global cellular consequences of LRRK2$_{G2019S}$ mutation in
312 conditions of iron overload we returned to our initial proteomics approach. We obtained the total
313 proteome from three biological replicates of wild type and LRRK2$_{G2019S}$ cells in untreated
314 conditions, and following 24 hours of FAS treatment (**Supplemental Table 2**). While FAS
315 treatment induced many expected changes in wild type cells, including reduced transferrin
316 receptor, increased ferritins, there were many more robust changes in FAS treated LRRK2$_{G2019S}$
317 cells relative to their wild type counerparts (**Supplemental Table 2, Volcano Plot in Figure**
318 **4A**). GO analysis highlighted three functional groups that included changes in oxidative stress

319 related genes, in lysosomal proteins, and cytoskeletal signatures (**Figure 4B**). For example,
320 proteomics identified a 10 $_{Log2}$fold increase in Heme Oxygenase 1 (HMOX1) in LRRK2$_{G2019S}$
321 cells treated with FAS compared to wild type cells, which we validated by western blot
322 comparing to both wild type and LRRK2KO cells (**Supplementary Figure 4A**). This is a well
323 studied transcriptional target of NRF2 and part of the canonical oxidative stress response.
324 Consistent with this, we also observed the nuclear translocation of NRF2 specifically in
325 LRRK2$_{G2019S}$ FAS treated cells (**Supplementary Figure 4B,C**), and a block in cellular
326 proliferation (**Supplementary Figure 4D**). These data indicate a significant increase in oxidative
327 stress within mutant cells in the context of iron overload.
328 We were surprised to identify a reduction in Monoamine Oxidase A (MAOA) in
329 LRRK2$_{G2019S}$ cells, which we validated by western blot (**Supplementary Figure 4A**). However,
330 while specific to the LRRK2$_{G2019S}$, the loss of MAOA was seen in both untreated and iron
331 overloaded LRRK2$_{G2019S}$ macrophages, indicating that, while it is a very interesting observation,
332 the loss of MAOA is unrelated to the iron phenotypes under investigation here. An outer
333 membrane enzyme primarily studied in neurons where it acts to degrade monoamine
334 neurotransmitters like serotonin, dopamine and epinephrine (Naoi et al., 2025), its induced
335 expression in tumor associated macrophages has recently been shown to promote
336 immunosuppression that promotes tumour progression (Ma et al., 2024; Wang et al., 2021). We
337 also checked the specificity of another candidate, the RNA binding protein IGF2BP3 (insulin-
338 like growth factor 2 mRNA binding protein 3), which has been shown to regulate the mRNA
339 stability of both iron/stress related targets including HMOX1 (Lv et al., 2025), STEAP3 (Liang
340 et al., 2026), SLC7A11 (Yang et al., 2026) and FTH (Xu et al., 2022). In this case, the IGF2BP3
341 levels were highly upregulated in both LRRK2$_{G2019S}$ and the LRRK2KO lines, irrespective of
342 iron overload (**Supplementary Figure 4A**).
343 The second global signature showed a specific downregulation of a series of lysosomal
344 hydrolases including lysozymes and granzymes, with other lysosomal enzymes appearing to
345 increase in LRRK2$_{G2019S}$ iron treated cells (**Figure 4B**). To test the hydrolytic activity within
346 lysosomes in these conditions we employed a proteolytic sensor BSA-DQ$_{Red}$ that is internalized
347 into endolysosomes and becomes fluorescent upon cleavage by lysosomal hydrolyases (Marwaha
348 and Sharma, 2017). In steady state there was little difference in lysosomal hydrolytic activity in
349 LRRK2$_{G2019S}$ macrophages, relative to WT (**Figure 4C**). Upon iron overload we observe a ~50%
350 decrease in activity in control cells, as observed previously (Fernandez et al., 2016). This
351 decrease was exacerbated in LRRK2$_{G2019S}$ macrophages showing an ~90% reduction in
352 hydrolytic capacity reported by the probe (**Figure 4C**). This was not due to a lack of
353 acidification, as demonstrated by lysotracker probes that showed increased signal upon iron
354 overload in both genotypes (**Figure 4D**).
355 Together with the observation that the lysosomes within LRRK2$_{G2019S}$ cells do not
356 expand like they do in wild type cells upon iron overload, and that there is a block in NCOA4
357 microautophagy (**Figure 2**), the data indicate that the lysosomes within LRRK2$_{G2019S}$ iron loaded
358 cells are dysfunctional. Very recent work has suggested that lysosomes in LRRK2$_{G2019S}$ cells can
359 accumulate ferrous iron, which could promote lipid oxidation (Mamais et al., 2025). We
360 therefore employed the C11-Bodipy probe where the wavelength shifts to green upon the
361 oxidation of this lipid probe and observed an increased peroxidation of the probe within both
362 internal membranes and at the plasma membrane (**Figure 4E, quantified in F**). Upon costaining
363 with lysotracker deep red we further report the oxidized lipids localizing to lysosomal
364 membranes (**Figure 4G**). Iron-induced peroxidation of lipids is known to be a driver of

365 ferroptotic cell death. This can be detected upon uptake of SYTOX green, a dye added to the
366 media which enters cells upon rupture of the cell surface. Indeed, we observe ~50% of
367 LRRK2$_{G2019S}$ cells positive for SYTOX green following 48 hours of FAS treatment, while wild
368 type cells remained viable (**Figure 4G**).
369

370 ## Discussion

371 The literature describing pathogenic LRRK2 mutations in PD overwhelmingly supports a
372 model where a host of different mutations across the protein all result in a gain-of-function
373 kinase activity that has focused clinical trials on LRRK2 kinase inhibitors. Previous studies have
374 identified iron mishandling in LRRK2 mutant cells, and MRI approaches identify iron
375 accumulation as a biomarker in patient carriers of the mutation (Fernandez et al., 2022; Jia et al.,
376 2023; Khan et al., 2024; Mamais et al., 2025; Mamais et al., 2021; Martinez et al., 2023; Nazish
377 et al., 2023; Oun et al., 2022). This work supports previous studies and further highlights
378 dysregulated iron metabolism as a potential pathway of interest in LRRK2-related PD.
379 Our data indicate a primary dysfunction in lysosomal dynamics and function in iron
380 loaded LRRK2$_{G2019S}$ cells where they do not undergo lysosomal enlargement and begin to lose
381 hydrolytic activity. These organelles cannot promote the degradation of NCOA4, which then
382 accumulates in the cytosol within detergent-insoluble foci. The accumulation of peroxidated
383 C11-Bodipy within lysosomes is consistent with a recent preprint reporting that LRRK2$_{G2019S}$
384 cells accumulate Fe2+ within lysosomes that can results in lipid oxidation (Mamais et al., 2025).
385 Our data do not resolve the earliest mechansisms to explain why the kinase-active LRRK2
386 prevents the dynamic changes within lysosomes that are triggered by iron overload. However,
387 our experiments revelealed that the increased LRRK2$_{G2019S}$-dependent phosphorylation of Rab8
388 seen in iron overload was reversed only with a type II inhibitor, and was resistant to the type I
389 inhibitor MLi-2 even though the inhibitor engaged LRRK2$_{G2019S}$, as indicated by the loss of the
390 pS1292 autophosphorylation mark. These results suggest that iron treatment alters the
391 conformational landscape of LRRK2$_{G2019S}$ differently, which could reflect LRRK2 as an iron
392 binding protein, or that a new protein interaction occurs in high iron that alters the conformation
393 of the kinase domain. One study identified the NCOA4 ubiquitin ligase HERC2 as a LRRK2
394 binding protein (Imai et al., 2015), although no follow-up studies have confirmed this. One
395 possibility is that LRRK2 could interfere with HERC2s capacity to degrade NCOA4.
396 In addition to this unusual feature of LRRK2 in iron loaded cells, the appearance of p-
397 Rab8 at the plasma membrane was unexpected given the localization of LRRK2 has been
398 documented primarily at Golgi and lysosomes, particularly upon lysosomal damage. It is
399 possible that this reflects LRRK2 recruitment to the plasma membrane damage following the
400 increase in oxidized lipids, perhaps in an effort to repair the membrane given that established
401 function of LRRK2 (Bentley-DeSousa et al., 2025). This would suggest that the cell surface
402 pRab8 reflects a downstream consequence of altered lysosomal response to iron overload. Future
403 experiments will focus on the potential function of LRRK2 at the cell surface and whether this
404 localization could explain the differential sensitivity to the type I and type II kinase inhibitors.
405 Lastly, our experiments are limited to a cultured macrophage RAW cell line. It is
406 important to note that the impact of LRRK2$_{G2019S}$ mutations on steady state iron homeostasis
407 appears to be highly cell and context specific. It was our proteomics analysis that initially
408 identified the loss of FTH and increased FTL within LRRK2$_{G2019S}$ RAW macrophages. However
409 scRNAseq experiments from LRRK2$_{G2019S}$ mice showed that most cell types had no alteration in
410 iron related genes, with the noted exception of microglia, some astrocyte cell types and

411 oligodendrocytes, with neurons showing no change (Khan et al., 2024). Functional experiments
412 examining iron homeostasis in LRRK2 heterozygous mutant iPSC derived lines have also seen
413 changes in ferrous iron accumulation in lysosomes(Mamais et al., 2025), and in mice showing an
414 induction of iron dysregulation in microglia upon LPS treatment (Mamais et al., 2021). In this
415 context our work adds some critical new insight into the consequence of the kinase active
416 LRRK2 on the processes of ferritinophagy, and degradation of NCOA4, highlighting an
417 unexpected localization of p-Rab8 to the plasma membrane. Future work will resolve the
418 underlying mechanisms and context specific actions of LRRK2 in iron metabolism. For now we
419 expand the experimental foundation for further exploration of LRRK2s impact in conditions of
420 iron overload. Given the historical focus on iron toxicity within the *substantia nigra pars*
421 *compacta* and *locus cerulean* of PD patients, this may be an important physiological niche where
422 LRRK2 mutations may play pathological roles. With the ongoing clinical trials focused on
423 LRRK2 kinase inhibitors it will be important to monitor their efficacy with biomarkers linked to
424 iron metabolism, perhaps including quantitative susceptibility mapping MRI (Guan et al., 2024;
425 Martinez et al., 2023).
426

427
428 ## Materials and Methods
429
430 ### *Cell culture and reagents*
431 RAW264.7 cells WT (Cat# TIB-71, RRID:CVCL_0493), RAW264.7 LRRK2-G2019S (RRID:
432 CVCL_F1ZX), RAW264.7 mCherry-FTL (RRID:CVCL_F2A0), RAW264.7 mCherry-NCOA4
433 (RRID:CVCL_F2A2), RAW264.7 TMEM192-HA (RRID:CVCL_F2A4) and RAW264.7
434 LRRK2-KO (RRID: CVCL_F1ZZ) were cultured in DMEM containing high glucose, GLUTA-
435 PLUS and sodium pyruvate (Wisent 319-027-CL) supplemented with 10% heat inactivated fetal
436 bovine serum (Wisent 098159) and antibiotics (Gibco 15-140-122). Cells were cultured at 37°C
437 and 5% CO2 in a humidified incubator and regularly tested for mycoplasma.
438
439 Bafilomycin A1 (B1793), Ammonium iron (II) sulfate hexahydrate (FAS) (09719),
440 Deferroxamine mesylate salt (DFO) (D9533) and LLOME (L7393) were purchased from
441 Millipore-Sigma, MLi-2 was purchased from Abcam (ab254528). Rebastinib was purchased
442 from MedChemExpress (HY-13024), while Rn277 and Rn341 were kindly provided by Samara
443 Reck-Peterson and Andres Leschziner (Weill Cornell Medicine, NY).
444
445 ### *$LRRK2_{G2019S}$ proteomics analysis*
446 Samples were reconstituted in 50 mM ammonium bicarbonate with 10 mM TCEP [Tris(2-
447 carboxyethyl) phosphine hydrochloride (T2556, Thermo Fisher Scientific), and vortexed for 1 h
448 at 37°C. Chloroacetamide (C0267, Sigma-Aldrich) was added for alkylation to a final
449 concentration of 55 mM. Samples were vortexed for another hour at 37°C. One microgram of
450 trypsin was added, and digestion was performed for 8 h at 37°C. Samples were dried down and
451 solubilized in 5% ACN-4% formic acid (FA). The samples were loaded on a 1.5 µl pre-column
452 (Optimize Technologies, Oregon City, OR). For each run, 1µg of peptides were separated on an
453 home-made reversed-phase column (150-µm i.d. by 200 mm) with a 116-min gradient from 10 to
454 30% ACN-0.2% FA and a 600-nl/min flow rate on a Easy nLC-1200 connected to a Exploris 480
455 (Thermo Fisher Scientific, RRID:SCR_022215) with the FAIMS interface. Each proteome was
456 analyzed with 4 separate LC-MS/MS runs acquired with a different set of compensation voltages
457 (CV) and a different m/z range: run1 was performed with the CV set-44V-54V-64V-74V from
458 m/z 350 to 453, run 2 was performed wdith the CV set -40V-48V-56V-64V-72V-80V from m/z
459 451 to 542, run 3 was performed with the CV set -40V-48V-56V-64V-72V-80V from m/z 540 to
460 661, run 4 was performed with the CV set -35V-46V-57V from m/z 659 to 890. Each full MS
461 spectrum acquired at a resolution of 120,000 was followed by tandem-MS (MS-MS) spectra
462 acquisition on the most abundant multiply charged precursor ions for 3s. Tandem-MS
463 experiments were performed using higher energy collision dissociation (HCD) at a collision
464 energy of 34% with an AGC of 50% a resolution of 15,000 and a injection time of 28ms. The
465 data were processed using PEAKS X Pro (Bioinformatics Solutions,
466 https://www.bioinfor.com/peaks-xpro/, RRID:SCR_022841) and a Uniprot mouse database
467 (16977 entries) with trypsin as digestion mode. Mass tolerances on precursor and fragment ions
468 were 10 ppm and 0.01 Da, respectively. Fixed modification was carbamidomethyl (C). Variable
469 selected posttranslational modifications were acetylation (N-ter), oxidation (M), deamidation
470 (NQ), phosphorylation (STY).
471

472 *Cell lysates, SDS-PAGE and immunoblotting*
473 Cells were collected by scraping, washed twice with cold PBS buffer and resuspended in X1
474 PBS containing protease inhibitors (Roche 04693132001) and phosphatase inhibitors (Roche
475 04906837001). Total protein content was quantified by Bradford assay (Bio-Rad 5000006) equal
476 quantities of samples were lysed in Laemmli buffer (10% (vol/vol) glycerol, 2% (wt/vol) SDS,
477 0.005% (wt/vol) bromophenol blue, 60 mMTris-HCl pH 6.8 and 10% (vol/vol) b-
478 mercaptoethanol), and heated 5 minutes at 95 °C prior loading into an SDS-PAGE. Proteins were
479 size separated and transferred to nitrocellulose membranes (Bio-Rad 1620097), blocked for one
480 hour in blocking solution (PBS-tween 0.5% (vol/vol) (PBS-T) containing 5% (w/v) skim milk).
481 After blocking, the membranes were incubated overnight (ON) with primary antibody solution
482 (1:1000 dilution of the antibodies in PBS-T unless otherwise specified). After primary antibody
483 incubation, membranes were washed five times for 10 minutes in PBS-T and incubated for one
484 hour with HRP conjugated secondary antibodies, Sheep anti-mouse (Cytiva, NA931,
485 RRID:AB_772210) and donkey anti-rabbit (Cytiva, NA934, RRID:AB_772206) in blocking
486 solution (1:5000). Finally, membranes were washed and developed using INTAS ChemoCam
487 (INTAS Science Imaging GmbH) using Western-Lightning PLUS-ECL (Revvity
488 NEL105001EA). Antibodies used in Western blots are as follows:
489 Rabbit Antibodies:
490 FTL (Proteintech 10727-1-AP, RRID:AB_2278673),
491 FTH (Cell Signaling 4393,RRID:AB_11217441),
492 LRRK2 (Abcam, ab133474, RRID:AB_2713963 or Abcam 133518, RRID:AB_2938806),
493 GAPDH (Santa Cruz, sc-25778,RRID:AB_10167668),
494 IRP2 (Proteintech, 29976-1-AP, RRID:AB_3086201),
495 p-LRRK2 s1292 (Abcam, ab203181, RRID:AB_2921223),
496 NCOA4 (Bethyl, A302-271A, RRID:AB_1850158),
497 TOMM40 (Proteintech, 18409-1-AP, RRID:AB_2303725),
498 Ferroportin (Alomone labs, AIT-001, RRID:AB_2340981),
499 p-Rab8A (1:250) (Abcam, ab230260, RRID:AB_2814988),
500 Rab8A (1:250) (Cell Signaling, cs-6975, RRID:AB_10827742),
501 AKT (Cell Signaling, cs-9272, RRID:AB_329827),
502 pAKT S473 (Cell Signaling, cs-4060, RRID:AB_2315049),
503 HMOX1 (Proteintech 10701-1-AP, RRID:AB_2122782),
504 MAOA (Proteintech 10539-1-AP, RRID:AB_2137251),
505 Igf2bp3 (Proteintech 10539-1-AP, RRID:AB_2137251),
506 Mouse Antibodies:
507 TfR (Invitrogen 136800, RRID:AB_2533029),
508 HERC2 (BD Bioscience, 612366, RRID:AB_399728),
509 FBXL5 (Santa Cruz, sc-390102),
510 DMT1 (SLC-11A2) (Santa Cruz, sc-166884, RRID:AB_10610255),
511 beta-actin (Santa Cruz, sc-8432, RRID:AB_626630),
512 PCNA ((Thermo Fisher Scientific Cat# 13-3900, RRID:AB_2533016),
513 vinculin (Sigma, V4505, RRID:AB_477617)
514 alpha-tubulin (Santa Cruz, sc-23948, RRID:AB_628410).
515

516 *Iron quantification*
517 Fe^{2+}, Fe^{3+} and total iron content was quantified using colorimetric Iron assay kit from Abcam
518 (ab83366) according to manufacturer instructions. Briefly, 2.5 x10^6 cells were seeded in 6 well
519 plate and treated with 100 µM FAS for 16 hrs. Each sample was lysed in 120 µl of assay buffer,
520 ad 50 µl were separated into two wells for quantification of Fe^{2+} and Fe^{3+} content. The rest of the
521 sample was kept for protein concentration estimation. Iron content was obtained by measuring
522 the Abs593 nm and the values were interpolated into the standard curve and then normalized to
523 protein concentration.
524
525 *Aconitase activity assay*
526 Aconitase activity was quantified using Abcam's colorimetric Aconitase activity assay kit
527 (ab83459), according to manufacturer's instructions. Briefly, 2.5 x10^6 cells were harvested,
528 washed with PBS and resuspended in Assay Buffer. Insoluble materials were cleared by
529 centrifuging samples at 800g, the resulting fraction was further centrifuged at 20.000 g for 15
530 minutes and the supernatant was utilized to quantify cytoplasmic aconitase activity. Aconitase
531 activity was measured colorimetrical by measuring absorbance 450 nm, and the enzymatic
532 activity calculated based on the standard curve and normalized to protein concentration.
533
534 *Generation of CRIPSR KI/KO and stable cell lines*
535 *$LRRK2_{G2019S}$ cell lines*
536 The gRNA for generation of homozygous $LRRK2_{G2019S}$ was designed using TrueDesign
537 Genome editor and synthesized by Thermo Fisher (sequence
538 U*U*G*CGAAGAUUGCGGACUAC + modified scaffold). The $LRRK2_{G2019S}$ HDR
539 template used was 5'- G*T*A*AACTTGTTCTCCTACCTGGGGTGC
540 CCTCTGATGTCTTTATTCCCATCCTGCAGCAGTACTGTGCGATCGAGTAGTCCGC
541 AATCTTCGCAATGATGGCAGCATTGGGATACAGGGTAAAAAGCAGCACATTGT
542 GGGGCTTCAGGTCACGGTAAATAATCATGGCTGAGTGG*A*G*A-3'. Raw cells
543 were scraped, washed with PBS and electroporated with Cas9 protein and donor HDR
544 templates using Neon transfection system (MPK5000, Thermo Fisher) according to the
545 manufacturer's instructions. After electroporation, cells were plated and cultured for 4 days.
546 Afterwards, single cells were seeded in 96 wells and genomic DNA was isolated from single
547 clones. The gRNA target region was amplified by PCR using AmpliTaq Gold 360 master mix
548 (4398881, Thermo Fisher). PCR amplicons were sequenced using standard Sanger
549 sequencing (Supp Fig 1A).
550
551 *Crispr KO of* LRRK2
552 To disrupt the LRRK2 loci, gRNAs were designed using the webtool CHOP CHOP
553 (https://chopchop.cbu.uib.no), and exons 1 and 7 of mouse *LRRK2* gene were targeted. sgRNA
554 exon1 GTGTTCACCTACTCGGACCGCGG and sgRNA exon 7
555 TGTCCGGTGCTACAATCTTGTGG were purchased from Synthego. Transfection was
556 performed according to manufacturer's instructions. Briefly, ribonucleoparticles (RNPs) were
557 assembled by incubating gRNAs with Cas9 enzyme, followed by reverse transfection using
558 lipofectamine RNAi max transfection reagent (Invitrogen, 13778150) diluted in Optimem (Gibco
559 31985070). Approximately 75,000 cells were seeded in a 24 well together RNPs-transfection
560 solution. 24 hours post transfection, single cells were seeded in 96 wells and several colonies

561 were monitored for the expression of LRRK2, one clone (D) was isolated with a two base pair
562 deletion ed in exon1 detected by Sanger sequencing.
563
564 *Stable cell lines*
565 Stable cells lines expressing mCherry-FTL and mCherry-NCOA4 were generated using
566 retroviral transduction system and stably integrated into the genome. Using Gateway system
567 (11791019, Thermo Fisher), cDNAs of FTL (subcloned from Addgene #100153), NCOA4
568 (DNASU HsCD00043681) https://dnasu.org/DNASU/Home.do, were cloned into a pBABE-
569 puro-mCherrry-GTW, which was engineered by cloning mCherry2 (Addgene # 54563) into
570 pBABEpuro-gateway (Addgene # 51070). For the generation of the retroviral particles, HEK293
571 phoenix cells (ATCC, CRL-3213, RRID:CVCL_H716) were transfected with the different
572 constructs using jetPrime transfection reagent (Polyplus 101000027). Media of the cells was
573 collected 48 hours post-transfection, 0.45 µm filtered and transduced into the macrophages. After
574 24 hours of viral transduction, media was changed and cells selected with 10 µg/ml puromycin
575 until the appearance of resistant colonies. Stable cell lines were used as polyclones.
576
577 Macrophage cells stably expressing TMEM192-HA (Addgene # 102930) were generated using
578 lentivirus. Lentiviral particles were generated in HEK293T cells using the Lenti-X packaging
579 (Takara 631275) according to manufacturer instructions. After 36 hours media was collected,
580 0.45 µm filtered and added to the RAW macrophages. 24 hours post-transduction cells were
581 selected in 10 µg /ml puromycin until the appearance of resistant colonies. TMEM192-HA
582 expression was confirmed by western blot, and polyclonal cell lines were used in this study.
583
584 *Immunofluorescence and live imaging conditions*
585 Cells were seeded in 13 mm sterile glass coverslips (Thermo Scientific 174950), fixed with 6%
586 PFA for 20 min at 37 °C, washed three times with PBS, and permeabilized with 0.1% Triton X-
587 100 in PBS for 20 minutes. After permeabilization, cells were blocked for 30 min at room
588 temperature in PBS 5% BSA and probed overnight 4 °C with primary antibodies. After
589 incubation with secondary antibody, slides were washed three additional times with PBS, stained
590 with DAPI (Invitrogen, D1306), washed with double distilled water. Finally, coverslips were
591 mounted on slides using fluorescent mounting media (Dako, S302380-2) prior to imaging.
592 Antibodies used in immunofluorescence are as follows:
593 Rabbit Antibodies:
594 LAMP1 (Abcam ab208943, RRID:AB_2923327),
595 p-RAB8 (Abcam, ab230260, RRID:AB_2814988)
596 NRF2 (Cell Signaling 12721, RRID:AB_2715528)
597 Mouse antibodies:
598 HA (Sigma H9658, RRID:AB_260092)
599 Rat antibodies:
600 LAMP1 (DSHB ab528127, RRID: AB_528127).
601
602 For pRAB8 staining, after PFA fixation, cells were permeabilized with ice cold methanol for 20
603 minutes at -20^{0}C before blocking. After washing primary antibodies, cells were incubated with
604 the appropriate secondary antibodies (1:3000), donkey anti rabbit coupled to Alexa 488
605 (Invitrogen, A11006, RRID:AB_2534114), coupled to Alexa 647 (Invitrogen, 21244,
606 RRID:AB_2535812), donkey anti rat coupled to Alexa 488 (Invitrogen, A11070,

607 RRID:AB_2534074), coupled to Alexa 647 (Invitrogen, 21247, RRID:AB_141778) or donkey
608 and mouse coupled to Alexa 488 (Invitrogen, A11029, RRID:AB_2534088).

609 For live imaging approximately 100,000 cells were seeded in glass bottom imaging plates
610 (Cellvis D35C4-20-1.5-N) and stained using normal growing media supplemented with 20 mM
611 HEPES for pH stabilization. For FerroOrange staining cells were incubated for 1 hour in 1 µM
612 FerroOrange (Dojindo F374), in complete media prior to imaging. For labeling late endosomes
613 and lysosomes, cells were incubated in 100 nM LysoTracker Green (Thermo Fisher Scientific,
614 L7526), LysoTrackerRed (Thermo Fisher Scientific, L7528) or LysoTracker far red (Thermo
615 Fisher Scientific, L12492) for 30 minutes prior to imaging. To quantify proteolytic activity
616 control or treated cells were incubated for 1 hour with 10 µg/mL BSA_{DQ} red (Thermo Fisher
617 Scientific, D12051) combined with 100 nM LysoTracker Green. For the assessment of lipid
618 peroxidation cells were incubated for 1 hour with 1µM Bodipy™ 581/591 C11 (Thermo Fisher
619 Scientific, D3861). For time lapse microscopy, a rate of 1 frame every 2 seconds was acquired.
620 After staining with different dyes and then imaged under controlled temperature and humidity
621 conditions. Cell death was assessed by staining the cells with 1 µM SYTOX Green (Thermo
622 Fisher Scientific, S34860). Immunofluorescence and live imaging experiment were acquired
623 using an Olympus IX83 inverted microscope (RRID:SCR_020344) with Yokogawa spinning
624 disk confocal microscope (RRID:SCR_020907) using an UPLANSAPO ×100/1.40 NA oil
625 objective an Andor iXon Ultra EMCCD camera (RRID:SCR_023166). All the samples were
626 measured under same acquisition and laser intensity conditions.

627 *Quantification of FTL subcellular distribution*
628 Distribution of cherry-FTL was classified into four categories: 1) *cytosolic* where most of FTL
629 signal was homogenously distributed across the cellular cytoplasm: 2) *lysosomal*, where the
630 brightest signal inside the cell colocalize with Lamp1 or lysotracker positive structures, 3)
631 *cytosolic and lysosomal*, where FTL signal is largely diffuse and dim structures positive for
632 Lamp1 or lysotracker could be detected, and 4) *cytosolic with condensates*, were FTL
633 distribution was largely diffuse and cytoplasmic but accumulation of bright Lamp1 or lysotracker
634 negative structures were detected.
635
636 *Biochemical fractionation of Triton X-100 soluble and insoluble fractions*
637 To fractionate triton soluble from insoluble fraction biochemically, cells were first resuspended
638 in PBS, protein concentration was estimated, equal amounts of different samples were
639 centrifuged at 600 g for 5 minutes, and cell pellets were resuspended in triton lysis buffer (50
640 mM HEPES pH7.4, 150 mM NaCl, 1%, triton X-100, 1 mM EDTA) supplemented with protease
641 and phosphatase inhibitors (referenced in cell lysate section). Cell lysates were vortexed
642 thoroughly and incubated for 10 minutes on ice followed by centrifugation at 20,000 x g, 4 °C
643 for 20 minutes. Supernatant was transferred to a fresh tube and diluted in Laemmli buffer to
644 generate 1X triton soluble fraction, while the remaining triton insoluble pellet was resuspended
645 in 1X Laemmli sample buffer to the same final volume of the soluble fraction. Samples were
646 then analyzed by SDS-PAGE.
647
648 *Quantification of condensate number and size with image analysis*
649 We used FIJI (http://fiji.sc, RRID:SCR_002285) to quantify the number and area of extra-
650 lysosomal condensates. Images of fixed cells expressing either mCherry-NCOA4, mCherry-FTL

651 or mCherry-FTH and Lamp1 lysosomal marker were acquired using the same laser and exposure
652 conditions and analyzed with the following workflow. This is a cell-based analysis, so first step
653 single cells were selected with a ROI, while the rest of the field was excluded from the analysis.
654 Next, the Lamp1 channel was selected, background subtracted and binarized by automatic
655 thresholding using Otsu method, to obtain a lysosomal mask. Using this lysosomal mask, particle
656 analysis was performed and the ROIs obtained were overlayed with the channel of interest
657 (mCherry- NCOA4, mCherry-FTL or mCherry-FTH), and all the pixels inside this ROIs
658 (lysosomes) were deleted. Finally, the resulting image of the channel of interest was again
659 background subtracted and binarized by automatic thresholding to obtain a mask which was then
660 particle analyzed to quantify the number and size of extra-lysosomal structures.
661

662 *Quantification of FerroOrange and Bodipy c11 integrated fluorescence intensity*

663 FerroOrange or Bodip1 c11 fluorescence intensity were quantified using live cells using confocal
664 microscopy and quantified by image analysis using FIJI, several cells per field were selected and
665 their integrated fluorescence intensity was measured. The experiment was repeated 4 times
666

667 *Quantification of lysosomal size and number with image analysis*

668 We used FIJI to analyze and quantified the number and size of lysosomes in single planes. It is
669 important to note that RAW macrophages are not flat cells, thus this number only represents the
670 single plane information and not the total cellular volume. For the analysis of lysosomes in
671 $LRRK2_{G2019S}$ macrophages we used cells expressing TMEM192-HA due to its high levels of
672 expression and clear distribution in the lysosomal membrane allowing better edge detection.
673 Briefly, images were acquired under the same laser power and time exposure conditions and
674 afterwards analyzed with the following workflow. First step, single cells were selected with a
675 ROI while the rest of the field was excluded from the analysis. Next, HA/LTG channel was
676 selected, background subtracted and binarized by automatic Otsu thresholding to obtain a
677 lysosomal mask. Using this lysosomal mask, particle analysis was performed, and the average
678 number and size of lysosomes was recorded per each studied cell.
679

680 *Quantification of lysosomal proteolytic activity by flow cytometry*

681 Cells were seeded and treated with 100 µM FAS for 48 hrs or left untreated for control. To
682 quantify lysosomal proteolytic activity cells were stained with 10 µg/ml of DQ-BSA red and 100
683 nM LysoTracker Green for 1 hour, under the same conditions described in live imaging section.
684 After staining, cells were collected and transferred to a fresh tube in a suspension of $1x10^6$ cells/
685 ml. For acquisition, single cell suspensions were acquired on an Attune NxT
686 (RRID:SCR_019590, Thermo Fisher). CS&T performance tracking was done prior to cell
687 acquisition by manufacturer's recommendation. PMT voltages were determined by Daily CS&T
688 performance tracking. Compensation controls were also acquired. 50 000 events were acquired
689 per sample. Finally, median DQ-BSA red fluorescence and median LysoTracker Green
690 fluorescence from three different repetitions is shown.
691

692 *Quantification of pRAB8 and NRF2 subcellular distribution*

693 Quantification of pRAB8 and NRF2 distribution was performed qualitatively. Briefly, control or
694 FAS treated cells were stained with endogenous antibodies, and signals from the channel
695 corresponding to the studied protein were equally thresholded among all the cell lines and
696 treatments. The number of cells displaying bright detectable pRAB8 signal at the plasma

membrane or NRF2 signal at the nucleus were counted as positive and the total number of cells assessed by DAPI nuclear staining was used to estimate the percentage of positive stained cells. Experiments were repeated at least three times with a minimum of 30 cells per condition.

Growth curves

To assess growth, on day 0, 150.000 cells were seeded in 12 well plates, and on day 1 cells were either left untreated for control or incubated with 100 µM FAS, quadruplicates measurements were performed in each condition, and cell number was followed for the period of 72 hours.

Statistical analysis

All experiments were performed independently at least three times and quantifications and/or representative images are provided. For each condition a minimum of 30 cells were analyzed in all biological replicates. One-way ANOVA statistical analysis was performed using the GraphPad Prism software (http://www.graphpad.com/, version 8.4.3, RRID:SCR_002798). Experiments with more than two samples included the multiple comparison analysis. The arithmetic mean with standard deviation of at least three independent experiments are depicted. In addition, the values of all individual cells and the mean of each experiment are shown for the quantifications of size and number of condensates as well as lysosomes. No statistical method was used to predetermine the sample size. The experiments were not randomized; the investigators were not blinded to allocation during experiments and outcome assessment.

Acknowledgements

We thank Rodolfo Zunino and all members of lab for their help throughout the study. We thank the Desjardins ASAP team and Austen Milnerwood (McGill) for critical comments on the manuscript. We are grateful to Dr. Shawn M Ferguson (Yale) for sharing insightful datasets and discussions during the course of the study. Drs. Samara Reck-Peterson and Andres Leschiziner (Weill-Cornell) provided significant insight and discussion on the use of their new Type II kinase inhibitors for which we are profoundly grateful.

Funding

Aligning Science Across Parkinson's (MD, HMM)
The study is funded by the joint efforts of Aligning Science Across Parkinson's (ASAP-025171) initiative (to MD, HMM) and the Canadian Institutes of Health Research Project Grant 165999 (HMM). MJFF administers the grant on behalf of ASAP and itself. For the purpose of open access, the author has applied a CC BY public copyright license to all Author Accepted Manuscripts arising from this submission.

Author contributions

Conceptualization: AG, MD, HMM
Methodology: AG, MN, RZ, JL, AF, YZX, ES, PT, CT, AM
Investigation: AG, MN, JL
Visualization: AG, HMM
Funding acquisition: HMM
Project administration: HMM
Supervision: HMM

742 Writing – original draft: AG, HMM
743 Writing – review & editing: AG, MN, MD, HMM
744
745 Competing interests: Authors declare that they have no competing interests
746

747 Data and materials availability:

748 The data, protocols (uploaded to protocols.io), and key lab materials used and generated in this
749 study are listed in a Key Resource Table alongside their persistent identifiers at
750 https://doi.org/10.5281/zenodo.19374070. Proteomics Data are available via ProteomeXchange
751 with identifier PXD071594. No code was generated in this study.

752 An earlier version of this manuscript was posted to BioRxiv at
753 **doi:** https://doi.org/10.1101/2025.08.25.672135.

754 ## References

755

756 Alessi, D.R., and S.R. Pfeffer. 2024. Leucine-Rich Repeat Kinases. *Annu Rev Biochem*. 93:261-
757 287.
758 Aravindan, A., M.E. Newell, and R.U. Halden. 2024. Literature review and meta-analysis of
759 environmental toxins associated with increased risk of Parkinson's disease. *Sci Total*
760 *Environ*. 931:172838.
761 Beinert, H., and M.C. Kennedy. 1993. Aconitase, a two-faced protein: enzyme and iron
762 regulatory factor. *FASEB J*. 7:1442-1449.
763 Bentley-DeSousa, A., D. Clegg, and S.M. Ferguson. 2025. LRRK2, lysosome damage, and
764 Parkinson's disease. *Curr Opin Cell Biol*. 93:102482.
765 Buck, S.A., and L.H. Sanders. 2025. LRRK2-mediated mitochondrial dysfunction in Parkinson's
766 disease. *Biochem J*. 482:721-739.
767 Cannon, T., and S. Gruenheid. 2022. Microbes and Parkinson's disease: from associations to
768 mechanisms. *Trends in microbiology*. 30:749-760.
769 Chasteen, N.D., and P.M. Harrison. 1999. Mineralization in ferritin: an efficient means of iron
770 storage. *J Struct Biol*. 126:182-194.
771 Devos, D., O. Rascol, W.G. Meissner, A. Foubert-Samier, S. Lewis, C. Tranchant, M. Anheim,
772 D. Maltete, P. Remy, K. Eggert, H. Pape, C. Geny, P. Couratier, C. Carroll, R. Sheridan,
773 D. Burn, N. Pavese, J. Raw, D. Berg, O. Suchowersky, L.V. Kalia, A. Evans, S. Drapier,
774 T. Danaila, A. Schnitzler, J.C. Corvol, G. Defer, N.T. Temin, C. Fradette, F. Tricta, C.
775 Moreau, and g. a Parkinson's disease study. 2025. Therapeutic modalities of deferiprone
776 in Parkinson's disease: SKY and EMBARK studies. *J Parkinsons Dis*. 15:72-86.
777 Di Maio, R., E.K. Hoffman, E.M. Rocha, M.T. Keeney, L.H. Sanders, B.R. De Miranda, A.
778 Zharikov, A. Van Laar, A.F. Stepan, T.A. Lanz, J.K. Kofler, E.A. Burton, D.R. Alessi,
779 T.G. Hastings, and J.T. Greenamyre. 2018. LRRK2 activation in idiopathic Parkinson's
780 disease. *Sci Transl Med*. 10.
781 Dowdle, W.E., B. Nyfeler, J. Nagel, R.A. Elling, S. Liu, E. Triantafellow, S. Menon, Z. Wang,
782 A. Honda, G. Pardee, J. Cantwell, C. Luu, I. Cornella-Taracido, E. Harrington, P. Fekkes,
783 H. Lei, Q. Fang, M.E. Digan, D. Burdick, A.F. Powers, S.B. Helliwell, S. D'Aquin, J.
784 Bastien, H. Wang, D. Wiederschain, J. Kuerth, P. Bergman, D. Schwalb, J. Thomas, S.
785 Ugwonali, F. Harbinski, J. Tallarico, C.J. Wilson, V.E. Myer, J.A. Porter, D.E. Bussiere,
786 P.M. Finan, M.A. Labow, X. Mao, L.G. Hamann, B.D. Manning, R.A. Valdez, T.
787 Nicholson, M. Schirle, M.S. Knapp, E.P. Keaney, and L.O. Murphy. 2014. Selective
788 VPS34 inhibitor blocks autophagy and uncovers a role for NCOA4 in ferritin degradation
789 and iron homeostasis in vivo. *Nat Cell Biol*. 16:1069-1079.
790 Fell, M.J., C. Mirescu, K. Basu, B. Cheewatrakoolpong, D.E. DeMong, J.M. Ellis, L.A. Hyde, Y.
791 Lin, C.G. Markgraf, H. Mei, M. Miller, F.M. Poulet, J.D. Scott, M.D. Smith, Z. Yin, X.
792 Zhou, E.M. Parker, M.E. Kennedy, and J.A. Morrow. 2015. MLi-2, a Potent, Selective,
793 and Centrally Active Compound for Exploring the Therapeutic Potential and Safety of
794 LRRK2 Kinase Inhibition. *J Pharmacol Exp Ther*. 355:397-409.
795 Fernandez, B., E. Fdez, P. Gomez-Suaga, F. Gil, I. Molina-Villalba, I. Ferrer, S. Patel, G.C.
796 Churchill, and S. Hilfiker. 2016. Iron overload causes endolysosomal deficits modulated
797 by NAADP-regulated 2-pore channels and RAB7A. *Autophagy*. 12:1487-1506.

798 Fernandez, B., P. Olmedo, F. Gil, E. Fdez, Y. Naaldijk, P. Rivero-Rios, F. Bracher, C. Grimm,
799 G.C. Churchill, and S. Hilfiker. 2022. Iron-induced cytotoxicity mediated by
800 endolysosomal TRPML1 channels is reverted by TFEB. *Cell death & disease*. 13:1047.
801 Galy, B., M. Conrad, and M. Muckenthaler. 2024. Mechanisms controlling cellular and systemic
802 iron homeostasis. *Nat Rev Mol Cell Biol*. 25:133-155.
803 Gardet, A., Y. Benita, C. Li, B.E. Sands, I. Ballester, C. Stevens, J.R. Korzenik, J.D. Rioux, M.J.
804 Daly, R.J. Xavier, and D.K. Podolsky. 2010. LRRK2 is involved in the IFN-gamma
805 response and host response to pathogens. *J Immunol*. 185:5577-5585.
806 Guan, X., M. Lancione, S. Ayton, P. Dusek, C. Langkammer, and M. Zhang. 2024.
807 Neuroimaging of Parkinson's disease by quantitative susceptibility mapping.
808 *Neuroimage*. 289:120547.
809 Herbst, S., P. Campbell, J. Harvey, E.M. Bernard, V. Papayannopoulos, N.W. Wood, H.R.
810 Morris, and M.G. Gutierrez. 2020. LRRK2 activation controls the repair of damaged
811 endomembranes in macrophages. *EMBO J*. 39:e104494.
812 Imai, Y., Y. Kobayashi, T. Inoshita, H. Meng, T. Arano, K. Uemura, T. Asano, K. Yoshimi, C.L.
813 Zhang, G. Matsumoto, T. Ohtsuka, R. Kageyama, H. Kiyonari, G. Shioi, N. Nukina, N.
814 Hattori, and R. Takahashi. 2015. The Parkinson's Disease-Associated Protein Kinase
815 LRRK2 Modulates Notch Signaling through the Endosomal Pathway. *PLoS Genet*.
816 11:e1005503.
817 Jaimon, E., Y.E. Lin, F. Tonelli, O. Antico, D.R. Alessi, and S.R. Pfeffer. 2025. Restoration of
818 striatal neuroprotective pathways by kinase inhibitor treatment of Parkinson's disease-
819 linked LRRK2-mutant mice. *Sci Signal*. 18:eads5761.
820 Jenner, P. 1989. Clues to the mechanism underlying dopamine cell death in Parkinson's disease.
821 *J Neurol Neurosurg Psychiatry*. Suppl:22-28.
822 Jia, R., Y. Liu, K. Shuai, C. Zhou, L. Chen, L. Zhu, and X.M. Wu. 2023. The Relationship
823 between Iron and LRRK2 in a 6-OHDA-Induced Parkinson's Disease Model. *Int J Mol*
824 *Sci*. 24.
825 Johnson, M.E., B. Stecher, V. Labrie, L. Brundin, and P. Brundin. 2019. Triggers, Facilitators,
826 and Aggravators: Redefining Parkinson's Disease Pathogenesis. *Trends Neurosci*. 42:4-
827 13.
828 Kadgien, C.A., A. Kamesh, and A.J. Milnerwood. 2021. Endosomal traffic and glutamate
829 synapse activity are increased in VPS35 D620N mutant knock-in mouse neurons, and
830 resistant to LRRK2 kinase inhibition. *Mol Brain*. 14:143.
831 Khan, S.S., E. Jaimon, Y.E. Lin, J. Nikoloff, F. Tonelli, D.R. Alessi, and S.R. Pfeffer. 2024. Loss
832 of primary cilia and dopaminergic neuroprotection in pathogenic LRRK2-driven and
833 idiopathic Parkinson's disease. *Proc Natl Acad Sci U S A*. 121:e2402206121.
834 Kuno, S., H. Fujita, Y.K. Tanaka, Y. Ogra, and K. Iwai. 2022. Iron-induced NCOA4
835 condensation regulates ferritin fate and iron homeostasis. *EMBO Rep*. 23:e54278.
836 Leschziner, A.E., and S.L. Reck-Peterson. 2021. Structural Biology of LRRK2 and its
837 Interaction with Microtubules. *Movement disorders : official journal of the Movement*
838 *Disorder Society*. 36:2494-2504.
839 Li, X., H. Zhu, B.T. Huang, X. Li, H. Kim, H. Tan, Y. Zhang, I. Choi, J. Peng, P. Xu, J. Sun, and
840 Z. Yue. 2024. RAB12-LRRK2 complex suppresses primary ciliogenesis and regulates
841 centrosome homeostasis in astrocytes. *Nat Commun*. 15:8434.
842 Liang, Y.L., C.R. Zhong, J.Y. Wu, Z.J. Lin, Z. Lin, T.J. Yi, Z.P. Chen, H.L. Jin, J.D. Yu, Z.Y.
843 Lin, Y.L. Wan, and G.L. Li. 2026. USP10 promotes cell proliferation and gemcitabine

844 resistance in pancreatic cancer by the regulation of IGF2BP3-STEAP3. *Oncogene*.
845 45:383-397.
846 Lim, S.Y., A.H. Tan, A. Ahmad-Annuar, N.U. Okubadejo, K. Lohmann, H.R. Morris, T.S. Toh,
847 Y.W. Tay, L.M. Lange, S. Bandres-Ciga, I. Mata, J.N. Foo, E. Sammler, J.C.E. Ooi, A.J.
848 Noyce, N. Bahr, W. Luo, R. Ojha, A.B. Singleton, C. Blauwendraat, and C. Klein. 2024.
849 Uncovering the genetic basis of Parkinson's disease globally: from discoveries to the
850 clinic. *Lancet Neurol*. 23:1267-1280.
851 Lin, Y.E., E. Jaimon, F. Tonelli, and S.R. Pfeffer. 2025. Pathogenic LRRK2 mutations cause loss
852 of primary cilia and Neurturin in striatal parvalbumin interneurons. *Life Sci Alliance*. 8.
853 Lis, P., S. Burel, M. Steger, M. Mann, F. Brown, F. Diez, F. Tonelli, J.L. Holton, P.W. Ho, S.L.
854 Ho, M.Y. Chou, N.K. Polinski, T.N. Martinez, P. Davies, and D.R. Alessi. 2018.
855 Development of phospho-specific Rab protein antibodies to monitor in vivo activity of
856 the LRRK2 Parkinson's disease kinase. *Biochem J*. 475:1-22.
857 Luo, L., A.A. Wall, S.J. Tong, Y. Hung, Z. Xiao, A.A. Tarique, P.D. Sly, E. Fantino, M.P.
858 Marzolo, and J.L. Stow. 2018. TLR Crosstalk Activates LRP1 to Recruit Rab8a and
859 PI3Kgamma for Suppression of Inflammatory Responses. *Cell reports*. 24:3033-3044.
860 Lv, L., M. Hu, J. Li, R. Guo, M. He, P. Zhou, Y. Lei, M. Chen, Z. Liu, and S. Zhou. 2025.
861 Methyltransferase-like 3 mediates m6A modification of heme oxygenase 1 mRNA to
862 induce ferroptosis of renal tubular epithelial cells in acute kidney injury. *Free Radic Biol*
863 *Med*. 229:168-182.
864 Ma, Y., H. Chen, H. Li, Z. Zhao, Q. An, and C. Shi. 2024. Targeting monoamine oxidase A: a
865 strategy for inhibiting tumor growth with both immune checkpoint inhibitors and immune
866 modulators. *Cancer Immunol Immunother*. 73:48.
867 Madero-Perez, J., E. Fdez, B. Fernandez, A.J. Lara Ordonez, M. Blanca Ramirez, P. Gomez-
868 Suaga, D. Waschbusch, E. Lobbestael, V. Baekelandt, A.C. Nairn, J. Ruiz-Martinez, A.
869 Aiastui, A. Lopez de Munain, P. Lis, T. Comptdaer, J.M. Taymans, M.C. Chartier-Harlin,
870 A. Beilina, A. Gonnelli, M.R. Cookson, E. Greggio, and S. Hilfiker. 2018. Parkinson
871 disease-associated mutations in LRRK2 cause centrosomal defects via Rab8a
872 phosphorylation. *Mol Neurodegener*. 13:3.
873 Mamais, A., R.D. Batchelor, A. Chairmandurai, N. Subrahmanian, N. Maio, C.D. Vulpe, and
874 M.J. LaVoie. 2025. Parkinson's disease LRRK2 mutations dysregulate iron homeostasis
875 and promote oxidative stress and ferroptosis in human neurons and astrocytes.
876 *bioRxiv*:2025.2009.2026.678370.
877 Mamais, A., J.H. Kluss, L. Bonet-Ponce, N. Landeck, R.G. Langston, N. Smith, A. Beilina, A.
878 Kaganovich, M.C. Ghosh, L. Pellegrini, R. Kumaran, I. Papazoglou, G.R. Heaton, R.
879 Bandopadhyay, N. Maio, C. Kim, M.J. LaVoie, D.C. Gershlick, and M.R. Cookson.
880 2021. Mutations in LRRK2 linked to Parkinson disease sequester Rab8a to damaged
881 lysosomes and regulate transferrin-mediated iron uptake in microglia. *PLoS Biol*.
882 19:e3001480.
883 Mancias, J.D., L. Pontano Vaites, S. Nissim, D.E. Biancur, A.J. Kim, X. Wang, Y. Liu, W.
884 Goessling, A.C. Kimmelman, and J.W. Harper. 2015. Ferritinophagy via NCOA4 is
885 required for erythropoiesis and is regulated by iron dependent HERC2-mediated
886 proteolysis. *Elife*. 4.
887 Mancias, J.D., X. Wang, S.P. Gygi, J.W. Harper, and A.C. Kimmelman. 2014. Quantitative
888 proteomics identifies NCOA4 as the cargo receptor mediating ferritinophagy. *Nature*.
889 509:105-109.

890 Martinez, M., M. Ariz, I. Alvarez, G. Castellanos, M. Aguilar, J. Hernandez-Vara, N. Caballol,
891 A. Garrido, A. Bayes, D. Vilas, M.J. Marti, C. Catalonian Neuroimaging Parkinson's
892 disease, P. Pastor, C.O. de Solorzano, and M.A. Pastor. 2023. Brainstem neuromelanin
893 and iron MRI reveals a precise signature for idiopathic and LRRK2 Parkinson's disease.
894 *NPJ Parkinsons Dis*. 9:62.
895 Marwaha, R., and M. Sharma. 2017. DQ-Red BSA Trafficking Assay in Cultured Cells to Assess
896 Cargo Delivery to Lysosomes. *Bio Protoc*. 7.
897 Masaldan, S., A.I. Bush, D. Devos, A.S. Rolland, and C. Moreau. 2019. Striking while the iron is
898 hot: Iron metabolism and ferroptosis in neurodegeneration. *Free Radic Biol Med*.
899 133:221-233.
900 Mata, I., P. Salles, M. Cornejo-Olivas, P. Saffie, O.A. Ross, X. Reed, and S. Bandres-Ciga. 2023.
901 LRRK2: Genetic mechanisms vs genetic subtypes. *Handb Clin Neurol*. 193:133-154.
902 Melman, A., and F. Bou-Abdallah. 2020. Iron mineralization and core dissociation in
903 mammalian homopolymeric H-ferritin: Current understanding and future perspectives.
904 *Biochim Biophys Acta Gen Subj*. 1864:129700.
905 Mir, R., F. Tonelli, P. Lis, T. Macartney, N.K. Polinski, T.N. Martinez, M.Y. Chou, A.J.M.
906 Howden, T. Konig, C. Hotzy, I. Milenkovic, T. Brucke, A. Zimprich, E. Sammler, and
907 D.R. Alessi. 2018. The Parkinson's disease VPS35[D620N] mutation enhances LRRK2-
908 mediated Rab protein phosphorylation in mouse and human. *Biochem J*. 475:1861-1883.
909 Naoi, M., W. Maruyama, M. Shamoto-Nagai, and P. Riederer. 2025. Type A monoamine
910 oxidase; its unique role in mood, behavior and neurodegeneration. *J Neural Transm*
911 *(Vienna)*. 132:387-406.
912 Nazish, I., A. Mamais, A. Mallach, C. Bettencourt, A. Kaganovich, T. Warner, J. Hardy, P.A.
913 Lewis, J. Pocock, M.R. Cookson, and R. Bandopadhyay. 2023. Differential LRRK2
914 Signalling and Gene Expression in WT-LRRK2 and G2019S-LRRK2 Mouse Microglia
915 Treated with Zymosan and MLi2. *Cells*. 13.
916 Niwa, M., T. Hirayama, K. Okuda, and H. Nagasawa. 2014. A new class of high-contrast Fe(II)
917 selective fluorescent probes based on spirocyclized scaffolds for visualization of
918 intracellular labile iron delivered by transferrin. *Org Biomol Chem*. 12:6590-6597.
919 Ohshima, T., H. Yamamoto, Y. Sakamaki, C. Saito, and N. Mizushima. 2022. NCOA4 drives
920 ferritin phase separation to facilitate macroferritinophagy and microferritinophagy. *J Cell*
921 *Biol*. 221.
922 Oun, A., A. Soliman, M. Trombetta-Lima, A. Tzepapadaki, D. Tsagkari, A. Kortholt, and A.M.
923 Dolga. 2022. LRRK2 protects immune cells against erastin-induced ferroptosis.
924 *Neurobiol Dis*. 175:105917.
925 Peter, I., and W. Strober. 2023. Immunological Features of LRRK2 Function and Its Role in the
926 Gut-Brain Axis Governing Parkinson's Disease. *J Parkinsons Dis*. 13:279-296.
927 Raig, N.D., K.J. Surridge, M. Sanz-Murillo, V. Dederer, A. Kramer, M.P. Schwalm, N.M. Lattal,
928 L. Elson, D. Chatterjee, S. Mathea, T. Hanke, A.E. Leschziner, S.L. Reck-Peterson, and
929 S. Knapp. 2025. Type II kinase inhibitors that target Parkinson's disease-associated
930 LRRK2. *Sci Adv*. 11:eadt2050.
931 Riederer, P., T. Nagatsu, M.B.H. Youdim, M. Wulf, J.M. Dijkstra, and J. Sian-Huelsmann. 2023.
932 Lewy bodies, iron, inflammation and neuromelanin: pathological aspects underlying
933 Parkinson's disease. *J Neural Transm (Vienna)*. 130:627-646.
934 Rouault, T.A. 2006. The role of iron regulatory proteins in mammalian iron homeostasis and
935 disease. *Nature chemical biology*. 2:406-414.

936 Sanz Murillo, M., A. Villagran Suarez, V. Dederer, D. Chatterjee, J. Alegrio Louro, S. Knapp, S.
937 Mathea, and A.E. Leschziner. 2023. Inhibition of Parkinson's disease-related LRRK2 by
938 type I and type II kinase inhibitors: Activity and structures. *Sci Adv*. 9:eadk6191.
939 Singh, P.K., and M.M.K. Muqit. 2020. Parkinson's: A Disease of Aberrant Vesicle Trafficking.
940 *Annu Rev Cell Dev Biol*. 36:237-264.
941 Steger, M., F. Tonelli, G. Ito, P. Davies, M. Trost, M. Vetter, S. Wachter, E. Lorentzen, G.
942 Duddy, S. Wilson, M.A. Baptista, B.K. Fiske, M.J. Fell, J.A. Morrow, A.D. Reith, D.R.
943 Alessi, and M. Mann. 2016. Phosphoproteomics reveals that Parkinson's disease kinase
944 LRRK2 regulates a subset of Rab GTPases. *Elife*. 5.
945 Sulzer, D., J. Bogulavsky, K.E. Larsen, G. Behr, E. Karatekin, M.H. Kleinman, N. Turro, D.
946 Krantz, R.H. Edwards, L.A. Greene, and L. Zecca. 2000. Neuromelanin biosynthesis is
947 driven by excess cytosolic catecholamines not accumulated by synaptic vesicles. *Proc*
948 *Natl Acad Sci U S A*. 97:11869-11874.
949 Tansey, M.G., R.L. Wallings, M.C. Houser, M.K. Herrick, C.E. Keating, and V. Joers. 2022.
950 Inflammation and immune dysfunction in Parkinson disease. *Nature reviews.*
951 *Immunology*. 22:657-673.
952 Tasegian, A., F. Singh, I.G. Ganley, A.D. Reith, and D.R. Alessi. 2021. Impact of Type II
953 LRRK2 inhibitors on signaling and mitophagy. *Biochem J*. 478:3555-3573.
954 Tong, S.J., A.A. Wall, Y. Hung, L. Luo, and J.L. Stow. 2021. Guanine nucleotide exchange
955 factors activate Rab8a for Toll-like receptor signalling. *Small GTPases*. 12:27-43.
956 Wall, A.A., L. Luo, Y. Hung, S.J. Tong, N.D. Condon, A. Blumenthal, M.J. Sweet, and J.L.
957 Stow. 2017. Small GTPase Rab8a-recruited Phosphatidylinositol 3-Kinase gamma
958 Regulates Signaling and Cytokine Outputs from Endosomal Toll-like Receptors. *J Biol*
959 *Chem*. 292:4411-4422.
960 Wang, Y.C., X. Wang, J. Yu, F. Ma, Z. Li, Y. Zhou, S. Zeng, X. Ma, Y.R. Li, A. Neal, J. Huang,
961 A. To, N. Clarke, S. Memarzadeh, M. Pellegrini, and L. Yang. 2021. Targeting
962 monoamine oxidase A-regulated tumor-associated macrophage polarization for cancer
963 immunotherapy. *Nat Commun*. 12:3530.
964 Winn, N.C., K.M. Volk, and A.H. Hasty. 2020. Regulation of tissue iron homeostasis: the
965 macrophage "ferrostat". *JCI Insight*. 5.
966 Xu, X., J. Cui, H. Wang, L. Ma, X. Zhang, W. Guo, X. Xue, Y. Wang, S. Qiu, X. Tian, Y. Miao,
967 M. Wu, Y. Yu, Y. Xu, J. Wang, and Y. Qiao. 2022. IGF2BP3 is an essential N(6)-
968 methyladenosine biotarget for suppressing ferroptosis in lung adenocarcinoma cells.
969 *Mater Today Bio*. 17:100503.
970 Yang, Y., H. Ye, S. Qin, M. Lin, Y. Liu, and X. Li. 2026. M6A reader IGF2BP3 stabili1zes
971 SLC7A11 to antagonize ferroptosis and promote gastric tumorigenesis. *Cell Signal*.
972 139:112295.
973 Zhao, H., Y. Lu, J. Zhang, Z. Sun, C. Cheng, Y. Liu, L. Wu, M. Zhang, W. He, S. Hao, and K.
974 Li. 2024. NCOA4 requires a [3Fe-4S] to sense and maintain the iron homeostasis. *J Biol*
975 *Chem*. 300:105612.
976 Zhu, H., P. Hixson, W. Ma, and J. Sun. 2024. Pharmacology of LRRK2 with type I and II kinase
977 inhibitors revealed by cryo-EM. *Cell Discov*. 10:10.
978

979 ## Figure Legends
980
981 ### Figure 1: $LRRK2_{G2019S}$ RAW macrophages show changes in iron homeostasis
982 **A-** Western blot analysis on whole cell lysates of $pRAB8_{T72}$ and $pLRRK2_{S1292}$ in WT and
983 $LRRK2_{G2019S}$ macrophages control or treated with 1µM MLi-2 for 16 hours. Vinculin serves as
984 loading control. **B-** Densitometry analysis of pRab:Rab8 and pLRRK2:LRRK2 ratios from WT
985 or $LRRK2_{G2019S}$ macrophages control or treated with 1µM MLi-2 . Band intensities of three
986 separate experiment and standard deviation (SD) are shown. **C**-Volcano plot showing
987 differentially expressed proteins in $LRRK2_{G2019S}$ compared to WT macrophages. On the x axis
988 fold change (FC) and in the y axis -log base 10 of the adjusted statistical significance (p.adj) are
989 plotted. Dashed lines represent the cut-offs for analysis, proteins with a fold change larger than -
990 /+ 1-fold and p.adj greater than 1.3 ($p<0.05$) were considered as differentially expressed. Red
991 dots depict some of the differentially expressed proteins important for iron metabolism. **D** – Heat
992 map and table depicting the fold change and the role of the main iron related proteins
993 differentially expressed in $LRRK2_{G2019S}$ macrophages. FC= fold change. Data found in
994 Supplementary Table 1. **E**- Western blot analysis on whole cell lysates of iron markers in WT
995 and $LRRK2_{G2019S}$ macrophages. GAPDH serves as loading control. **F**- Levels of ferric (Fe^{3+}) and
996 ferrous (Fe^{2+}) iron in WT and LRRK2 $_{G2019S}$ macrophages. Iron is quantified as µmoles of iron
997 per mg of protein. Prior to iron quantification, cells were fed overnight with 100 µM ferrous
998 ammonium sulfate (FAS). The means of three separate experiment are shown. **G**- Representative
999 images of cherry-FTL distribution in WT and $LRRK2_{G2019S}$ macrophages control or treated with
1000 DFO 250 µM for 24 hours. Lysosomes were stained with 100nM lysotracker green. Scale bar 4
1001 µm, inset 1µm. **H**- Qualitative classification of cherry-FTL distribution shown in G. The means
1002 of three separate experiment are shown. **I**- Western blot analysis of NCOA4, FTL and FTH and
1003 TfR levels on whole cell lysates of WT and $LRRK2_{G2019S}$ macrophages, control or treated for 24
1004 hours with 250 µM DFO. PCNA serves as loading control. Black arrow indicates proteolytic
1005 cleavage product of FTL.
1006
1007 ### Supplementary Figure 1: $LRRK2_{G2019S}$ RAW macrophages show changes in iron homeostasis
1008 **A**- Confirmation by Sanger sequencing of LRRK2 G2019S knock in generation in Raw
1009 macrophages. **B**- Densitometry analysis of FTH, FTL and TfR levels in WT and $LRRK2_{G2019S}$
1010 macrophages. Band intensities of three separate experiment and standard deviation (SD) are
1011 shown. **C**- Representative images of WT and LRRK2 $_{G2019S}$ macrophages stained with
1012 Fe^{2+}sensor FerroOrange. Fluorescence intensity of the images was color coded using FIJIs
1013 thermal LUT. Scale bar 5 µm. **D**- Quantification of FerroOrange fluorescence intensity of data
1014 shown in B. The means and single values of three separate experiment and standard deviation
1015 (SD) are shown. T-test statistical analysis is shown. **E**- Western blot analysis on whole cell
1016 lysates of IRP2 FBXL5 HERC2, ferroportin (FPT) and DMT1 in WT and $LRRK2_{G2019S}$
1017 macrophages. GAPDH serves as loading control. **F**- Quantification of Aconitase activity in WT
1018 and $LRRK2_{G2019S}$ RAW macrophages, expressed as activity units per mg of protein. The means
1019 of three separate experiment and standard deviation (SD) are shown. T-test statistical analysis is
1020 shown. **G -** Densitometry analysis of FTL, TfR and NCOA4 levels in WT and $LRRK2_{G2019S}$
1021 macrophages control or treated for 24 hours with 250 µM DFO. Band intensities of three
1022 separate experiment and standard deviation (SD) are shown. .
1023

1024 Figure 2: LRRK2$_{G2019S}$ show defects in NCOA4 turnover upon iron overload
1025 **A**- Representative images of cherry-NCOA4 distribution in WT and LRRK2$_{G2019S}$ macrophages
1026 control or treated for 16 hours with FAS 100 µM. Lysosomes were stained with anti LAMP1
1027 antibody. Scale bar 4 µm, inset 1µm. **B**- Quantification of the average size of cytoplasmic
1028 cherry-NCOA4 condensates calculated as µm^2 per cell of data shown in A. The means and single
1029 values of three separate experiment and standard deviation (SD) are shown. Multiple
1030 comparison one-way ANOVA statistical analysis. **C**-Quantification of average number of
1031 cytoplasmic cherry-NCOA4 condensates per cell of data shown in A. The means and single
1032 values of three separate experiment and standard deviation (SD) are shown. Multiple
1033 comparison one-way ANOVA statistical analysis. **D**- Representative time-lapse sequences of
1034 cherry-NCOA4 condensates in WT and LRRK2$_{G2019S}$ macrophages treated for 48 hours with
1035 FAS 100 µM. Lysosomes were stained with Lysotracker green. Time-lapse experiments were
1036 acquired for 5 minutes, capturing both channels every 2 seconds. Scale bar 4 µm, inset 1µm. **E**-
1037 Western blot analysis of triton x-100 soluble and triton x-100 insoluble NCOA4 levels in WT
1038 and LRRK2$_{G2019S}$ RAW macrophages control or treated with 25 nM bafilomycin for 3 hours. **F**-
1039 Western blot analysis of NCOA4 on whole cell extracts of WT and LRRK2$_{G2019S}$ macrophages
1040 treated for 16 hours with FAS 100 µM and then treated with 1 µM MLi-2 for 8 hours in the
1041 absence of iron. Phosphorylation levels of LRRK2 on S1292 is used as positive control, actin
1042 serves as loading control.
1043
1044 Supplementary Figure 2:LRRK2$_{G2019S}$ show defects in NCOA4 turnover upon iron overload
1045 **A**- Representative images of cherry-FTL distribution in WT and LRRK2$_{G2019S}$ macrophages
1046 control or treated for 16 hours with FAS 100 µM. Lysosomes were stained with lysotracker
1047 green. Scale bar 4 µm, inset 1µm. **B**- Qualitative classification of cherry-FTL distribution of data
1048 shown in A. The means of three separate experiment are shown with at least 30 cells per
1049 condition. **C**- Representative images of lysosomal morphology of WT and LRRK2$_{G2019S}$
1050 macrophages control or treated for 24 or 48 hours with FAS 100 µM. Cells expressing
1051 TMEM192-HA in their lysosomal surface were stained with anti HA antibody. Scale bar 4 µm.
1052 **D**- Quantification of average number of lysosomes per cell of the experiment shown in C. The
1053 means and single values of three separate experiment are shown. Multiple comparison one-way
1054 ANOVA statistical analysis. **E**- Quantification of the average lysosomal size per cell of data
1055 shown in C. The means and single values of three separate experiment are shown. Multiple
1056 comparison one-way ANOVA statistical analysis. **F**- Western blot analysis of FTH and NCOA4
1057 levels on whole cell extracts of WT and LRRK2$_{G2019S}$ macrophages control or treated for 4, 8 or
1058 24 hours with 1 µM MLi-2. Phosphorylation levels of LRRK2 on S1292 were used as positive
1059 control, PCNA serves as loading control. **G-** Densitometry analysis of NCOA4 kinetics changes
1060 in LRRK2 G2019S treated with MLi-2. Band intensities of three separate experiment and
1061 standard deviation (SD) are shown. **H**- Representative images of lysosome morphology of WT
1062 and LRRK2$_{G2019S}$ macrophages treated for 48 hours with FAS 100 µM and then incubated for 8
1063 hours with 1 µM MLi-2 in the presence of iron. Lysosomes were stained with anti LAMP1
1064 antibody. Scale bar 5 µm.
1065
1066 Figure 3: LRRK$_{G2019S}$ impact on iron metabolism reveals differential sensitivies to type I and type II
1067 kinase inhibitors.
1068 **A**-Representative images of endogenous pRab8A distribution in WT, LRRK2$_{G2019S}$ and LRRK2
1069 KO macrophages control of treated for 24 hours with FAS 250 µM. Lysosomes were stained

1070 with anti LAMP1 antibody. Scale bar 10 µm, inset 5 µm. **B**- Quantification of the percentage of
1071 cells showing positive pRAB8 signal at plasma membrane. The means and standard deviation of
1072 three separate experiments are shown. Multiple comparison one-way ANOVA statistical
1073 analysis. **C**- Western blot analysis of p-Rab8 in WT and LRRK2$_{G2019S}$ macrophages control or
1074 treated with 1µM MLi-2 for two hours and then left untreated or exposed to FAS 250 µM in the
1075 presence of the inhibitor . Phosphorylation levels of LRRK2 on S1292 were used as positive
1076 control and actin serves as loading control. **D**- Densitometry quantification of data shown in C.
1077 Band intensities of three separate experiment and standard deviation (SD) are shown. **E**-
1078 Western blot analysis of p-Rab8 in WT and LRRK2$_{G2019S}$ macrophages control or treated with
1079 1µM rebastinib for two hours and then left untreated or exposed to FAS 250 µM in the presence
1080 of the inhibitor . PCNA serves as loading control. **F-** Representative images of endogenous
1081 pRab8A distribution in LRRK2$_{G2019S}$ macrophages pre-treated for 2hours with 1µM rebastinib or
1082 with 1µM MLi-2 and treated for 24 hours with FAS 250 µM in the presence of the inhibitor.
1083 DNA is stained with DAPI. Scale bar 10 µm. **G-** Quantification of the percentage of cells
1084 showing positive pRab8 signal at plasma membrane from the experiment shown in F. The means
1085 of three separate experiments are shown. Multiple comparison one-way ANOVA statistical
1086 analysis. **H**- Representative images of endogenous pRab8A distribution in LRRK2$_{G2019S}$
1087 macrophages pre-treated for 2hours with 5µM Rn277 or 5µM Rn341and treated for 24 hours
1088 with FAS 250 µM in the presence of the inhibitor. DNA is stained with DAPI. Scale bar 10 µm.
1089 **I-** Quantification of the percentage of cells showing positive pRab8 signal at plasma membrane
1090 from the experiment shown in H. The means of three separate experiments are shown. Multiple
1091 comparison one-way ANOVA statistical analysis. **J-** Western blot analysis of p-Rab8 in WT
1092 and LRRK2$_{G2019S}$ macrophages control and FAS treated. LRRK2$_{G2019S}$ macrophages were also
1093 treated with 5µM Rn277 and 5µM Rn341 for two hours and then left untreated or exposed to
1094 FAS 250 µM in the presence of the inhibitor. PCNA serves as loading control. **K-** Densitometry
1095 quantification of data shown in J. Band intensities of three separate experiment and standard
1096 deviation (SD) are shown.
1097

1098 Supplementary Figure 3: LRRK$_{G2019S}$ impact on iron metabolism reveals differential sensitivies to
1099 type I and type II kinase inhibitors.

1100 **A**-Western blot analysis of p-Rab8 in WT, LRRK2$_{G2019S}$ and LRRK2 KO macrophages control
1101 or treated with FAS 250 µM for 16 hours. Tubulin serves as loading control. **B**- Densitometry
1102 quantification of data shown in A. Band intensities of three separate experiment and standard
1103 deviation (SD) are shown. **C**- Western blot analysis of Rab8 or Rab10 levels in LRRK2$_{G2019S}$
1104 treated with non-targeting (NT), Rab8 (R8) or Rab10 (R10) siRNA. Vinculin serves as loading
1105 control. **D**-Representative images of endogenous pRab8A distribution in LRRK2$_{G2019S}$
1106 macrophages treated for 72 hours with NT, Rab8 or Rab10 siRNA and treated for 24 hours with
1107 FAS 250 µM. DNA is stained with DAPI. Scale bar 10 µm. **E**- Quantification of the percentage
1108 of cells showing positive pRab8 signal at plasma membrane of data shown in D. The means of
1109 three separate experiments are shown. Multiple comparison one-way ANOVA statistical
1110 analysis. **F**- Representative images of endogenous pRab8A distribution in mitotic WT
1111 macrophages. Nuclei are stained with DAPI. Scale bar 5 µm. **G**- Representative images of
1112 endogenous pRAB8A distribution in WT macrophages control of treated for 3 hours with
1113 LLOME 1 mM. Lysosomes were stained with anti LAMP1 antibody. Scale bar 5 µm. **H**-Western
1114 blot analysis of p-AKT S473 in WT, LRRK2$_{G2019S}$ and LRRK2$_{ARM}$ macrophages control or
1115 treated with 250 or 500 µM FAS for 24 hours. Vinculin serves as loading control. **I**-

1116 Densitometry quantification of data shown in H. Band intensities of three separate experiment
1117 and standard deviation (SD) are shown. **J**- Densitometry quantification of Western blot analysis
1118 of WT and LRRK2$_{G2019S}$ macrophages control or treated with 1µM rebastinib for two hours and
1119 then left untreated or exposed to FAS 250 µM for 16 hours in the presence of the inhibitor.
1120 Band intensities of three separate experiment and standard deviation (SD) are shown.
1121

1122 Figure 4: LRRK2$_{G2019S}$ cells are hypersensitive to iron induced oxidation and ferroptotic cell death.
1123 **A-**Volcano plot showing differentially expressed proteins in LRRK2$_{G2019S}$ compared to WT
1124 macrophages treated for 16 hours with 100 µM FAS. On the x axis fold change (FC) and in the y
1125 axis -log base 10 of the adjusted statistical significance (p.adj) are plotted. Dashed lines represent
1126 the cut-offs for analysis, proteins with a fold change larger than -/+ 2.5-fold and p.adj greater
1127 than 1.3 ($p<0.05$) were considered as differentially expressed. In red highlighted some of the
1128 confirmed hits shown in supplementary figure 4A. **B** – Heat maps depicting the fold change of
1129 proteins associated with oxidative stress, lysosomal function and cytoskeleton that are
1130 differentially expressed in iron treated LRRK2$_{G2019S}$ macrophages. FC= fold change. Raw data
1131 found in Supplementary Table 2. **C-**Flow cytometric measurement of median BSA-DQ red
1132 fluorescence intensity in WT and LRRK2$_{G2019S}$ macrophages control or treated for 48 hours with
1133 FAS 100 µM. The median of three separate experiment is shown. Multiple comparison one-way
1134 ANOVA statistical analysis. **D**- Flow cytometric measurement of median LTG fluorescence
1135 intensity in WT and LRRK2$_{G2019S}$ macrophages control or treated for 48 hours with FAS 100
1136 µM. The median of three separate experiment is shown. Multiple comparison one-way ANOVA
1137 statistical analysis. **E**- Representatice images of WT and LRRK2 G2019S macropghages treated
1138 for 24 hours with 250 µM FAS and incubated with 1µM C11-bodipy for the detection of
1139 peroxidated lipids. Scale bar 10 µm. **F**- Quantification of integrated fluorescence intensity of
1140 peroxidated C11-Bodipy. The means and single values of three separate experiment and standard
1141 deviation (SD) are shown. T-test statistical analysis is shown. **G**- Representative images of
1142 LRRK2 G2019S macropghages treated for 24 hours with 250 µM FAS and incubated with 1µM
1143 C11-bodipy for the detection of peroxidated lipids. Lysosomes were stained with lysotracker
1144 deep red (100 nM). Scale bar 10 µm, inset 1µm. **H**- Representative images of WT and LRRK2
1145 G2019S macropghages treated for 48 hours with 500 µM FAS and incubated with Sytox green to
1146 identify death cells. DIC images were used for total cell quantifiaction .Scale bar 100 µm. **I**-
1147 Quantification of data shown in H. Data shown as percentage of sytox green positive cells. The
1148 mean of three separate experiment is shown. Multiple comparison one-way ANOVA statistical
1149 analysis.
1150

1151 Supplementary Figure 4: LRRK2$_{G2019S}$ cells are hypersensitive to iron induced oxidation and
1152 ferroptotic cell death.
1153 **A**- Confirmative western blot analysis of selected differentially expressed proteins in iron treated
1154 LRRK2G2019S macrophages compared to WT cells exposed to the same conditions. HMOX-1
1155 (hemeoxidase-1). MAOA (monoamino oxidase), FPT (ferroportin). **B**- Representative images of
1156 endogenous NRF2 distribution in WT, LRRK2$_{G2019S}$ and LRRK$_{ARM}$ macrophages for 48 hours
1157 with FAS 100 µM. Cell nuclei were stained with DAPI, lysosomes were stained with anti
1158 LAMP1 antibody. Scale bar 10 µm. **C**- Quantification of the percentage of cells showing
1159 nuclear NRF2 translocation. The means and single values of three separate experiment are
1160 shown. T-test statistical analysis is shown. **D**- Growth curve of WT, LRRK2$_{G2019S}$ and LRRK2

$_{KO}$ macrophages. Cell count was followed for 3 days in the presence or absence of 100 μM FAS. Each point shows the average and standard deviation of 4 measurement.

Supplementary Data File 1:

Raw sequencing data covering LRRK2G2019S mutation in RAW macrophage

Supplementary Data File 2:

Raw sequencing data covering LRRK2KO mutation in RAW macrophage

Supplementary Table 1:

Proteomics dataset from LRRK2G2019S and wild type RAW macrophages.

Supplementary Table 2:

Proteomics dataset from LRRK2G2019S and wild type RAW macrophages FAS treated macrophages.

Supplementary Video 1:

Time-lapse imaging of NCOA4-Cherry foci seen within phase-separated foci entering an enlarged lysosome labeled with Lysotracker Green in wild type cells after 48 hours of 100uM FAS treatment.

Supplementary Video 2:

Time-lapse imaging of NCOA4-Cherry enlarged foci that do not become internalized within lysosomes labeled with Lysotracker Green in $LRRK2_{G2019S}$ cells after 48 hours of 100uM FAS treatment.

FIGURE 1

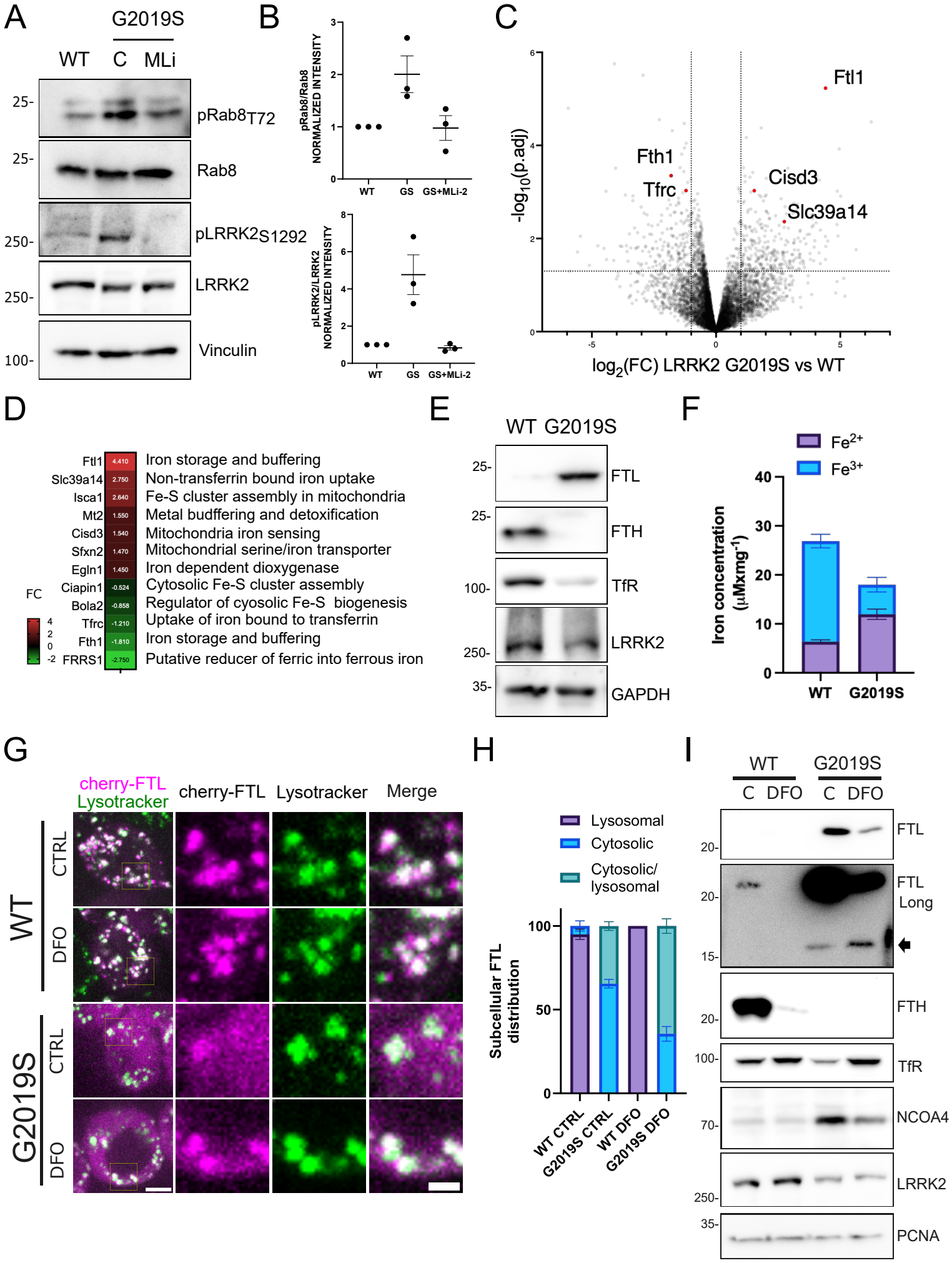
A
G2019S
WT
C
MLi
25-
pRab8T72
25-
Rab8
250-
pLRRK2S1292
250-
LRRK2
100-
Vinculin
B
pRab8/Rab8 NORMALIZED INTENSITY
WT
GS
GS+MLi-2
pLRRK2/LRRK2 NORMALIZED INTENSITY
C
Ftl1
Fth1
Tfrc
Cisd3
Slc39a14
-log10(p.adj)
log2(FC) LRRK2 G2019S vs WT
D
Ftl1 4.410 Iron storage and buffering
Slc39a14 2.750 Non-transferrin bound iron uptake
Isca1 2.640 Fe-S cluster assembly in mitochondria
Mt2 1.550 Metal budffering and detoxification
Cisd3 1.540 Mitochondria iron sensing
Sfxn2 1.470 Mitochondrial serine/iron transporter
Egln1 1.450 Iron dependent dioxygenase
Ciapin1 -0.524 Cytosolic Fe-S cluster assembly
Bola2 -0.858 Regulator of cyosolic Fe-S biogenesis
Tfrc -1.210 Uptake of iron bound to transferrin
Fth1 -1.810 Iron storage and buffering
FRRS1 -2.750 Putative reducer of ferric into ferrous iron
FC
E
WT G2019S
25-
FTL
25-
FTH
100-
TfR
250-
LRRK2
35-
GAPDH
F
Fe2+
Fe3+
Iron concentration (µMxmg-1)
WT
G2019S
G
cherry-FTL Lysotracker
cherry-FTL
Lysotracker
Merge
WT
CTRL
DFO
G2019S
CTRL
DFO
H
Lysosomal
Cytosolic
Cytosolic/ lysosomal
Subcellular FTL distribution
WT CTRL
G2019S CTRL
WT DFO
G2019S DFO
I
WT
G2019S
C
DFO
C
DFO
FTL
FTL Long
FTH
TfR
NCOA4
LRRK2
PCNA

SUPPLEMENTARY FIG1

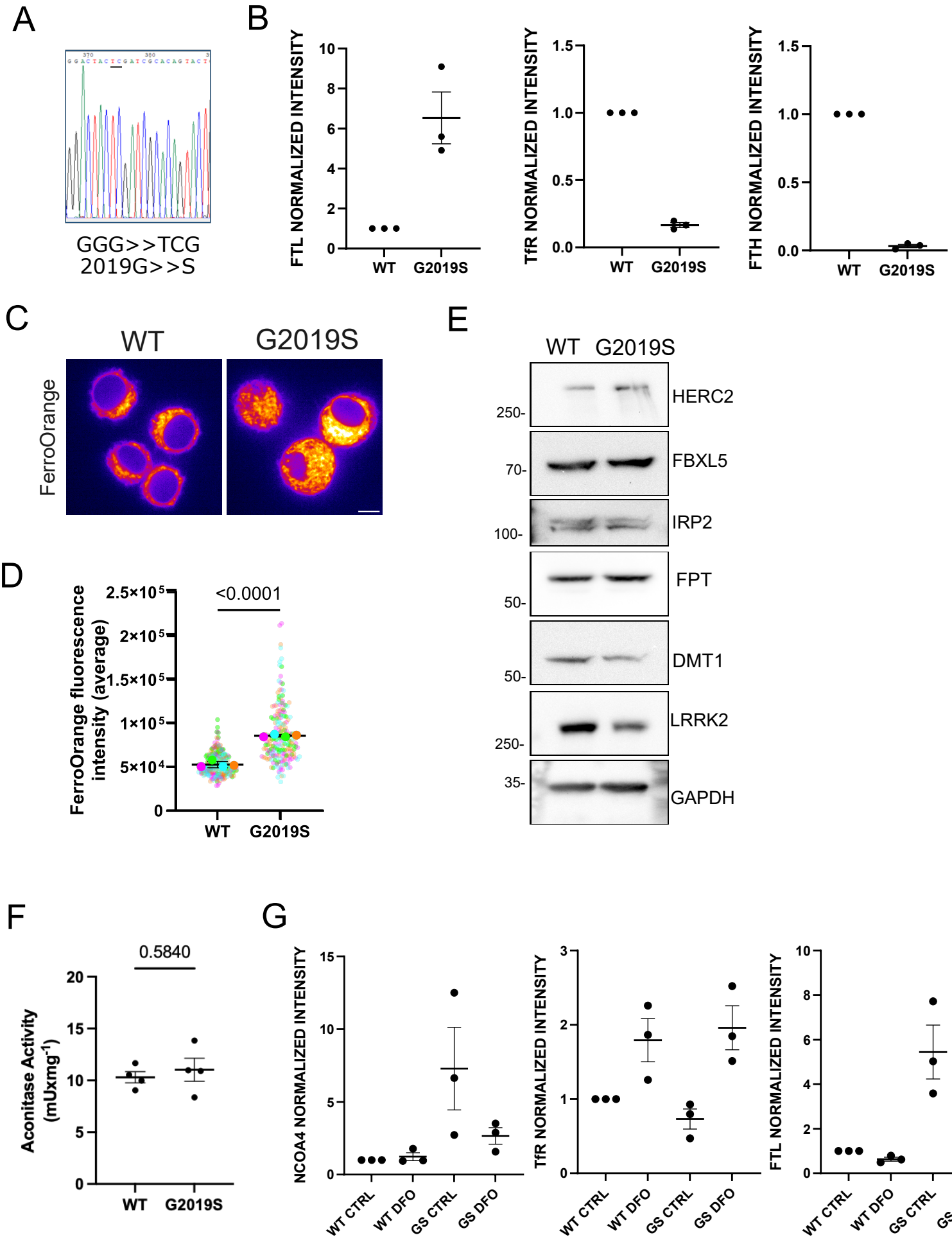

FIGURE2

A

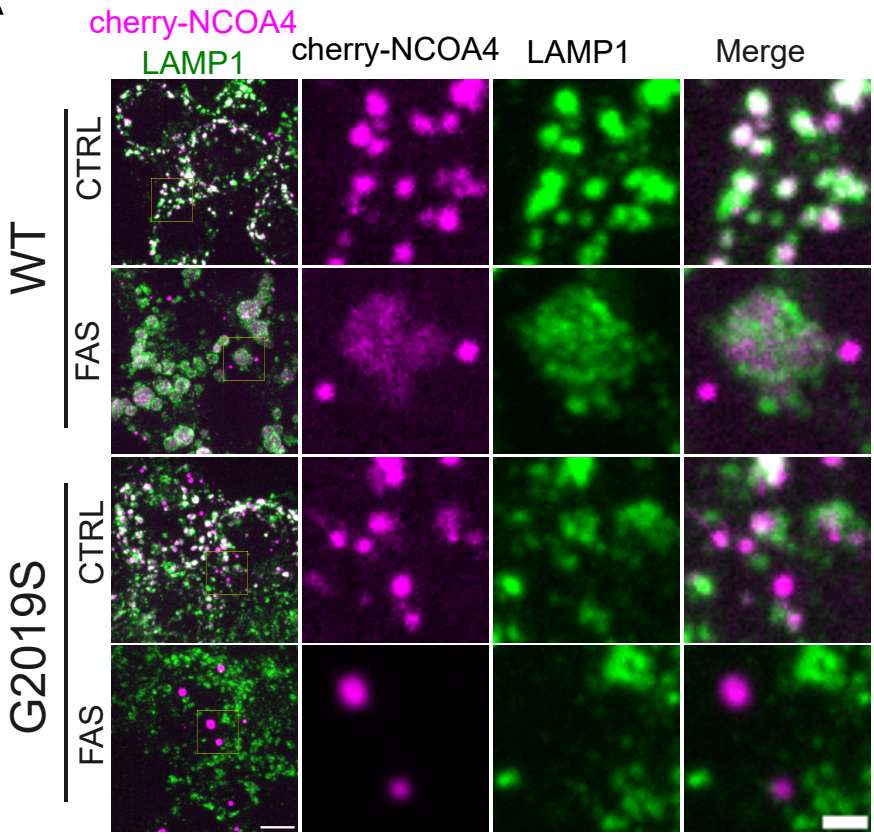

B

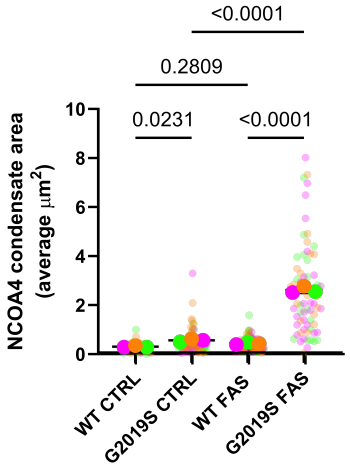

C

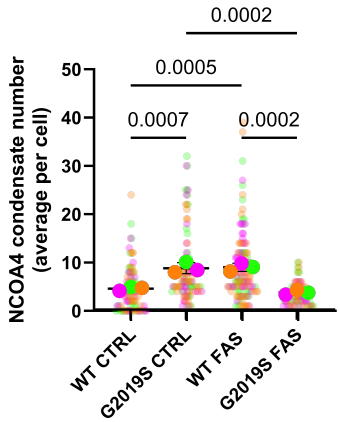

D

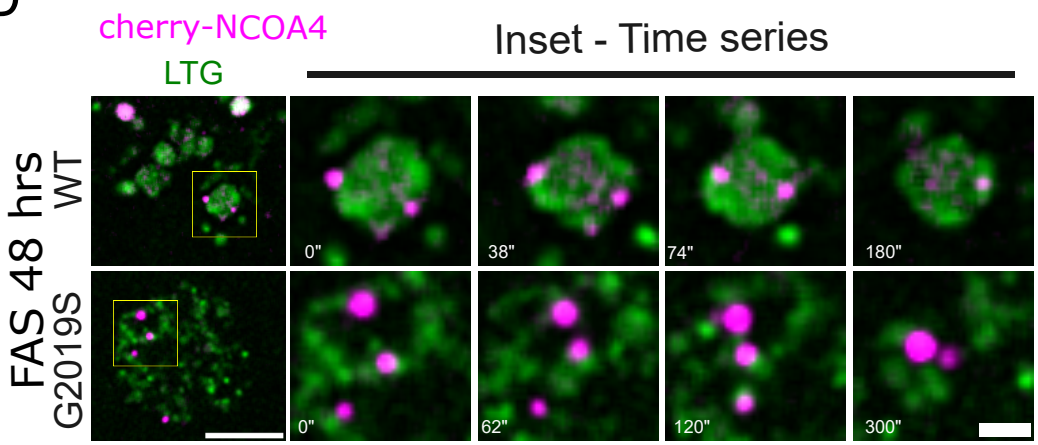

E

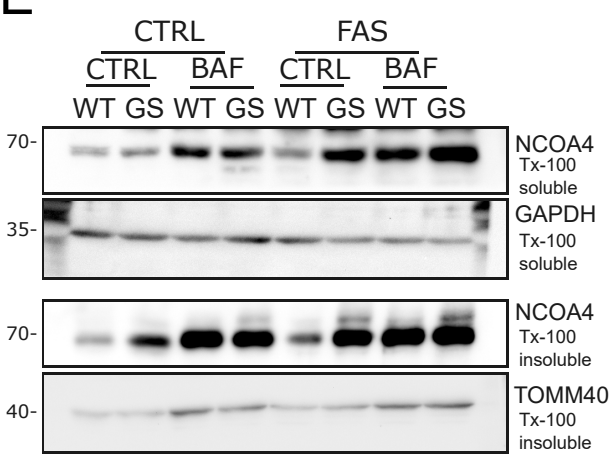

F

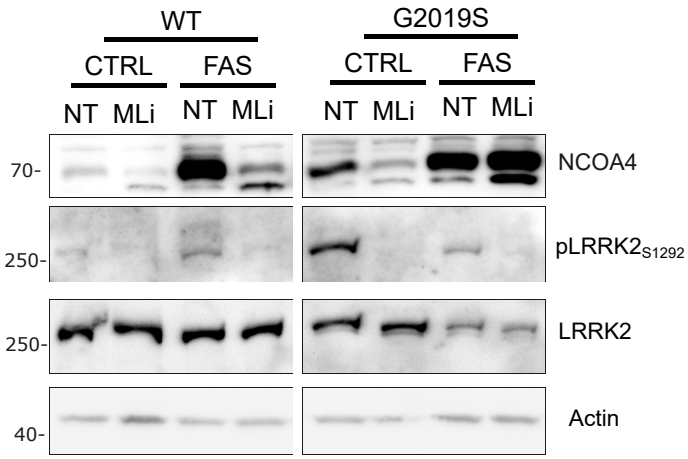

SUPPLEMENTARY FIG 2

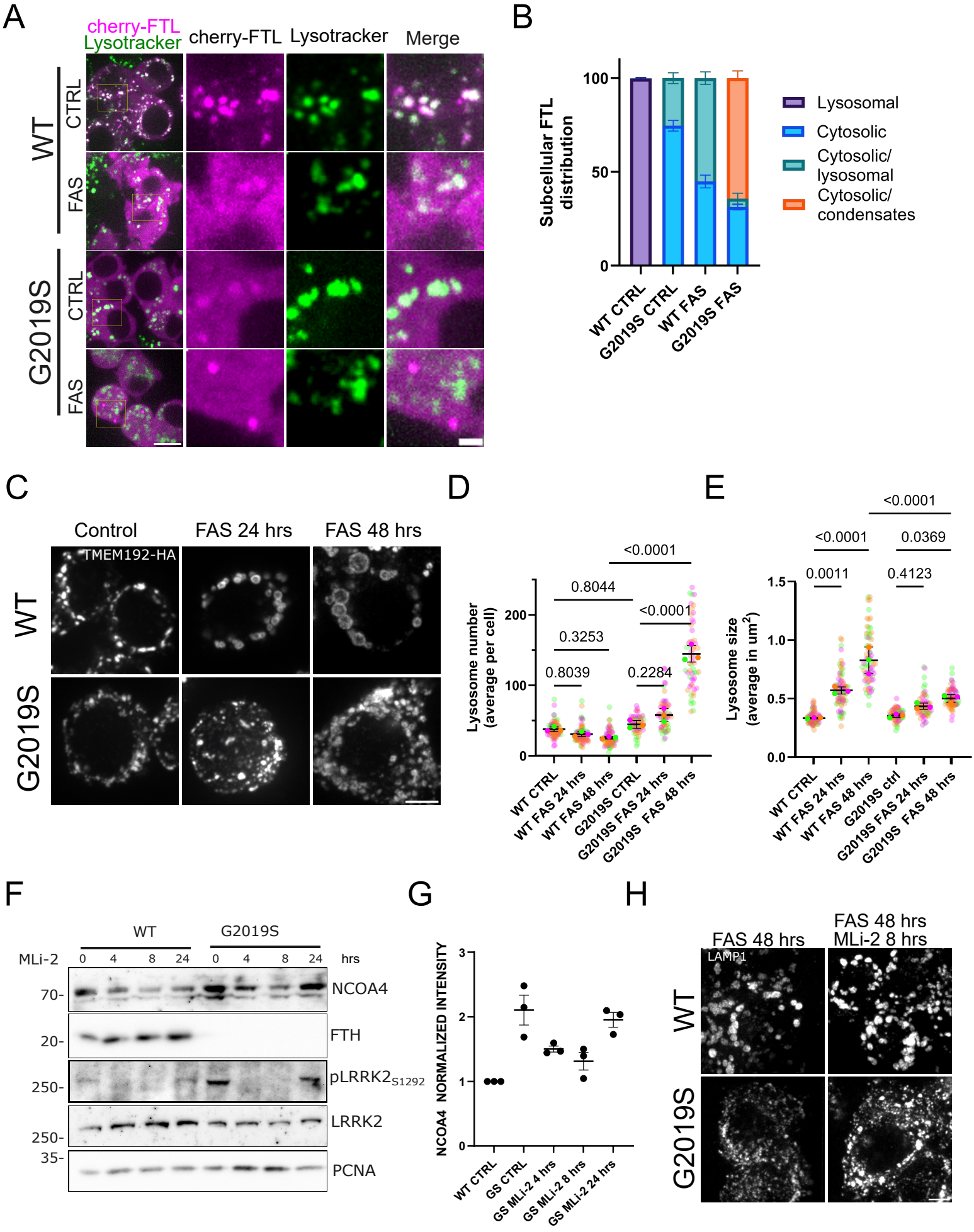

FIGURE 3

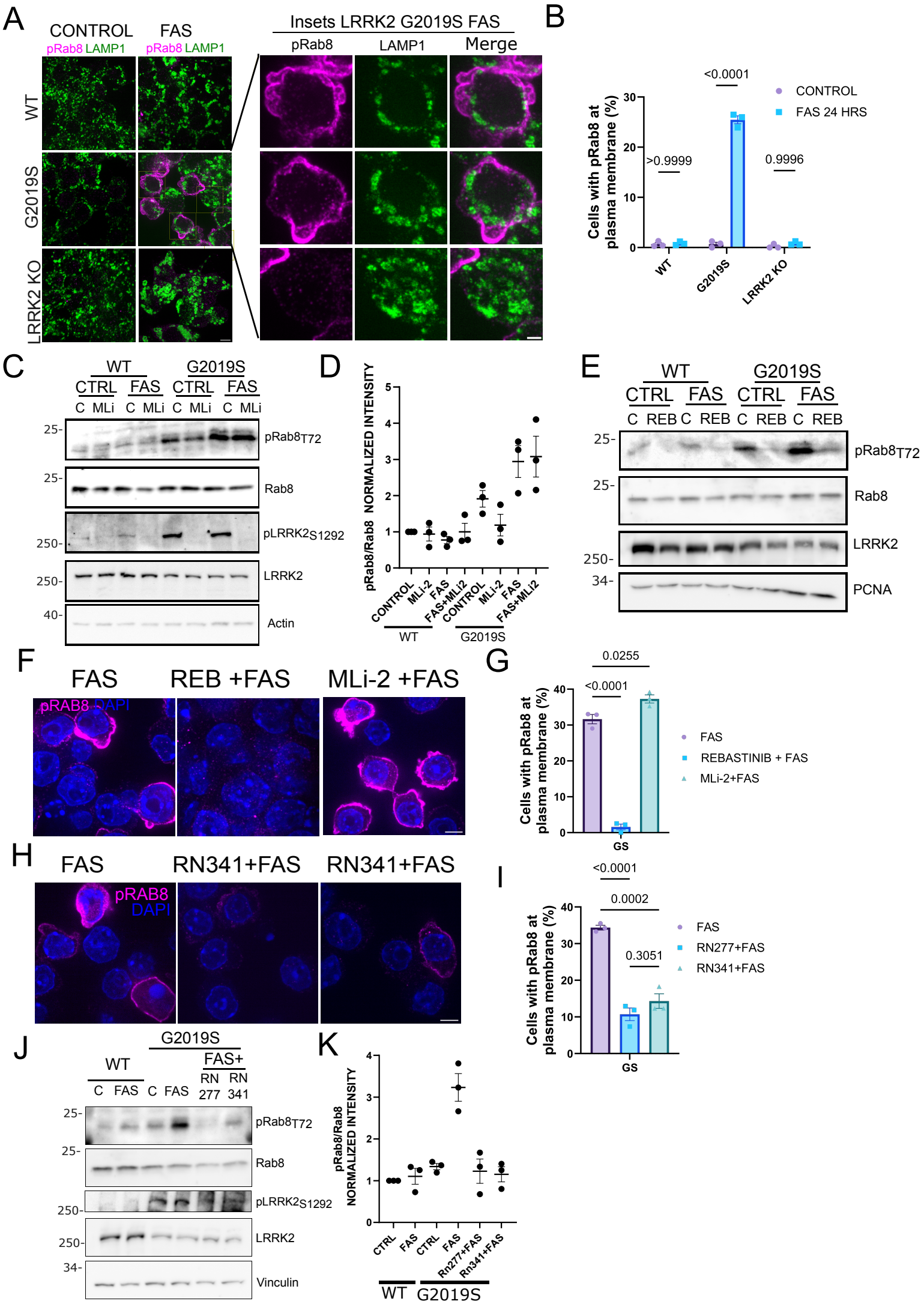
A
CONTROL
FAS
pRab8 LAMP1
pRab8 LAMP1
WT
G2019S
LRRK2 KO
Insets LRRK2 G2019S FAS
pRab8
LAMP1
Merge
B
Cells with pRab8 at plasma membrane (%)
<0.0001
>0.9999
0.9996
CONTROL
FAS 24 HRS
WT
G2019S
LRRK2 KO
C
WT
G2019S
CTRL
FAS
CTRL
FAS
C MLi C MLi C MLi C MLi
pRab8T72
Rab8
pLRRK2S1292
LRRK2
Actin
D
pRab8/Rab8 NORMALIZED INTENSITY
CONTROL
MLi-2
FAS
FAS+MLi2
CONTROL
MLi-2
FAS
FAS+MLi2
WT
G2019S
E
WT
G2019S
CTRL
FAS
CTRL
FAS
C REB C REB C REB C REB
pRab8T72
Rab8
LRRK2
PCNA
F
FAS
REB +FAS
MLi-2 +FAS
pRAB8 DAPI
G
0.0255
<0.0001
Cells with pRab8 at plasma membrane (%)
FAS
REBASTINIB + FAS
MLi-2+FAS
GS
H
FAS
RN341+FAS
RN341+FAS
pRAB8
DAPI
I
<0.0001
0.0002
0.3051
Cells with pRab8 at plasma membrane (%)
FAS
RN277+FAS
RN341+FAS
GS
J
G2019S
WT
FAS+
C FAS C FAS
RN 277
RN 341
pRab8T72
Rab8
pLRRK2S1292
LRRK2
Vinculin
K
pRab8/Rab8 NORMALIZED INTENSITY
CTRL
FAS
CTRL
FAS
Rn277+FAS
Rn341+FAS
WT
G2019S

SUPPLEMENTARY FIG 3

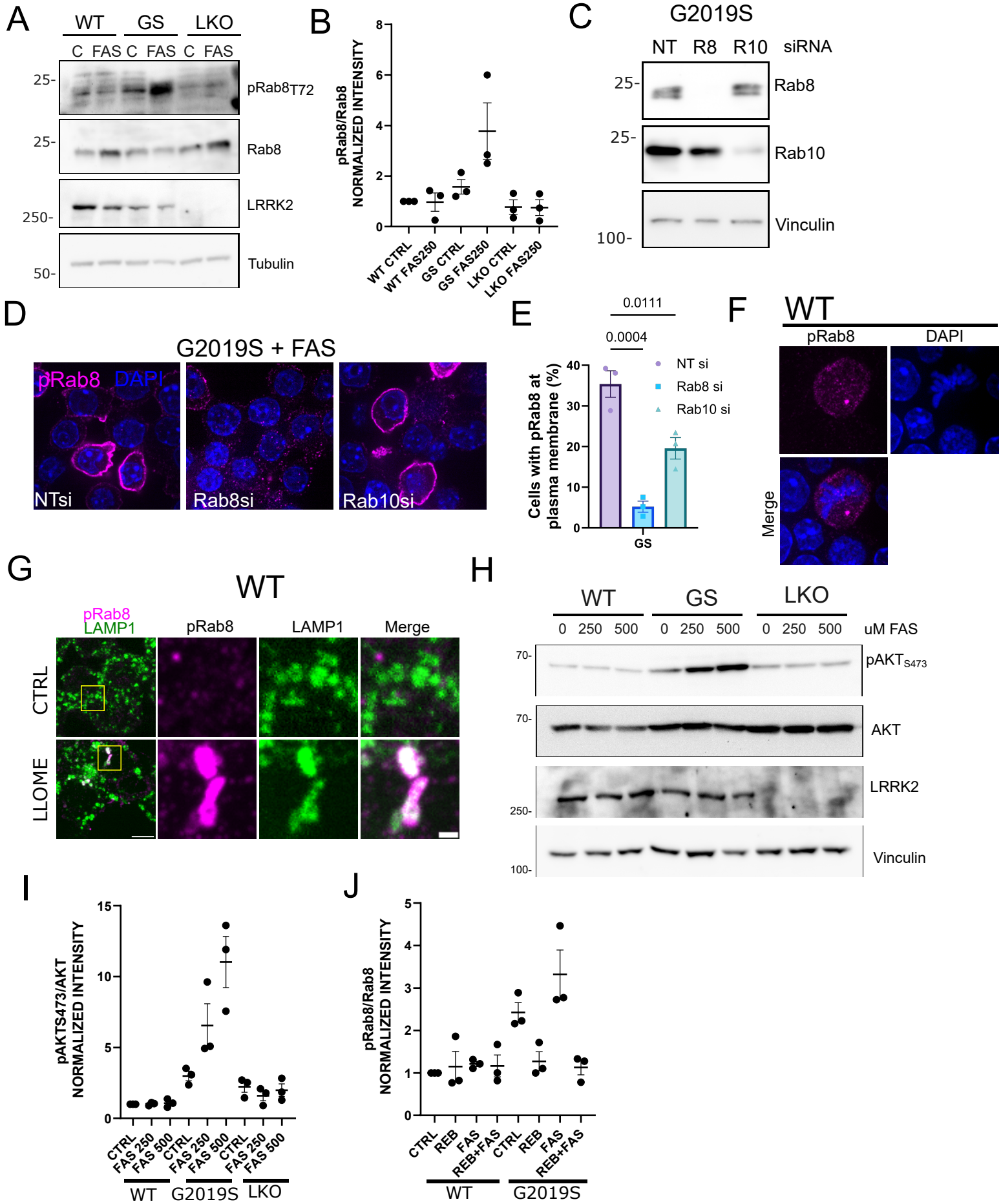

FIGURE 4

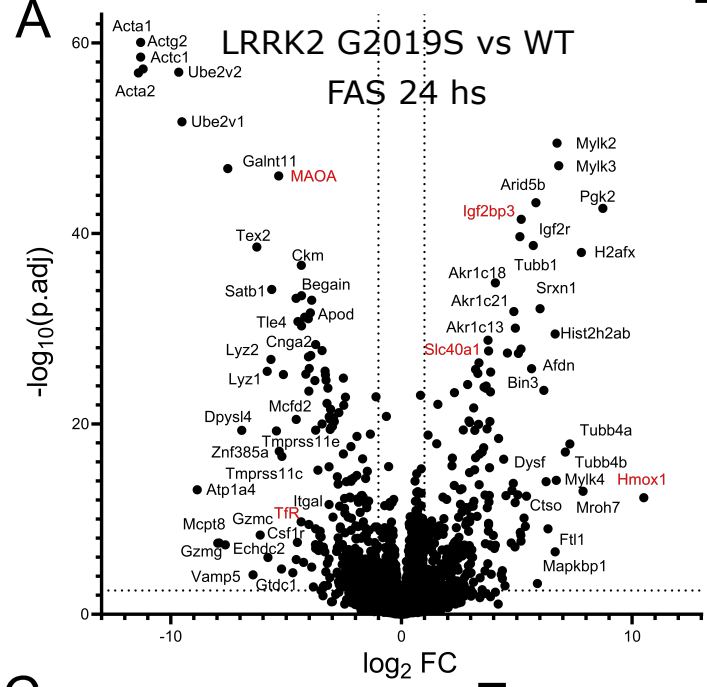
A
LRRK2 G2019S vs WT
FAS 24 hs
-log10(p.adj)
log2 FC
Acta1
Actg2
Actc1
Ube2v2
Acta2
Ube2v1
Galnt11
MAOA
Tex2
Ckm
Satb1
Begain
Apod
Tle4
Cnga2
Lyz2
Lyz1
Mcfd2
Dpysl4
Tmprss11e
Znf385a
Tmprss11c
Atp1a4
Itgal
Mcpt8
Gzmc
TfR
Csf1r
Gzmg
Echdc2
Vamp5
Gtdc1
Mylk2
Mylk3
Arid5b
Pgk2
Igf2bp3
Igf2r
H2afx
Tubb1
Akr1c18
Srxn1
Akr1c21
Akr1c13
Hist2h2ab
Slc40a1
Afdn
Bin3
Tubb4a
Dysf
Tubb4b
Mylk4
Hmox1
Ctso
Mroh7
Ftl1
Mapkbp1

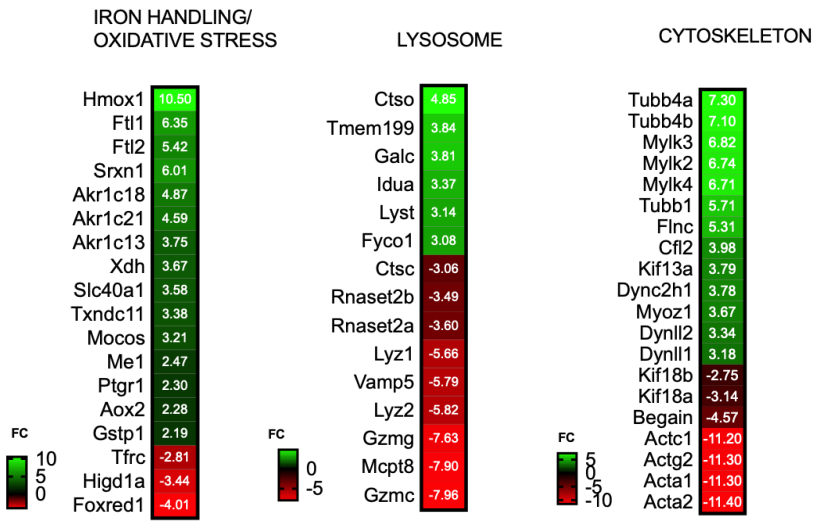
B
IRON HANDLING/ OXIDATIVE STRESS
Hmox1 10.50
Ftl1 6.35
Ftl2 5.42
Srxn1 6.01
Akr1c18 4.87
Akr1c21 4.59
Akr1c13 3.75
Xdh 3.67
Slc40a1 3.58
Txndc11 3.38
Mocos 3.21
Me1 2.47
Ptgr1 2.30
Aox2 2.28
Gstp1 2.19
Tfrc -2.81
Higd1a -3.44
Foxred1 -4.01
FC
LYSOSOME
Ctso 4.85
Tmem199 3.84
Galc 3.81
Idua 3.37
Lyst 3.14
Fyco1 3.08
Ctsc -3.06
Rnaset2b -3.49
Rnaset2a -3.60
Lyz1 -5.66
Vamp5 -5.79
Lyz2 -5.82
Gzmg -7.63
Mcpt8 -7.90
Gzmc -7.96
FC
CYTOSKELETON
Tubb4a 7.30
Tubb4b 7.10
Mylk3 6.82
Mylk2 6.74
Mylk4 6.71
Tubb1 5.71
Flnc 5.31
Cfl2 3.98
Kif13a 3.79
Dync2h1 3.78
Myoz1 3.67
Dynll2 3.34
Dynll1 3.18
Kif18b -2.75
Kif18a -3.14
Begain -4.57
Actc1 -11.20
Actg2 -11.30
Acta1 -11.30
Acta2 -11.40
FC

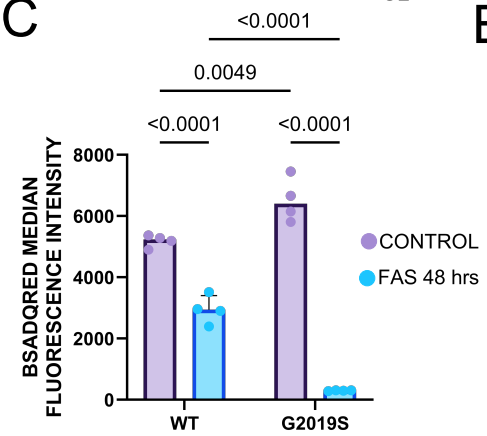
C
<0.0001
0.0049
<0.0001
<0.0001
BSADQRED MEDIAN FLUORESCENCE INTENSITY
CONTROL
FAS 48 hrs
WT
G2019S

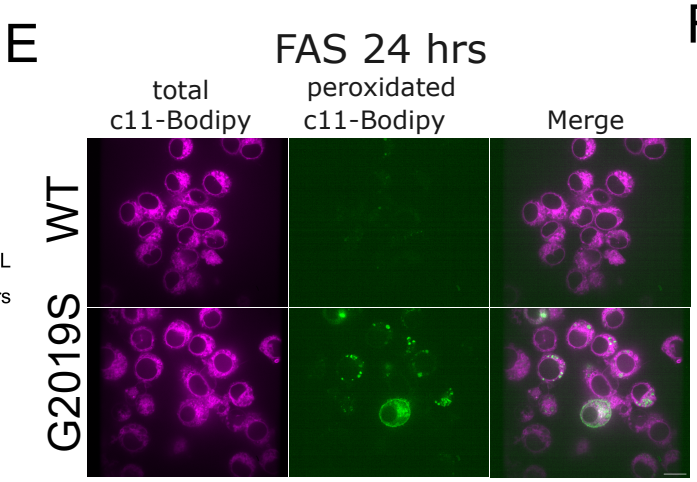
E
FAS 24 hrs
total c11-Bodipy
peroxidated c11-Bodipy
Merge
WT
G2019S

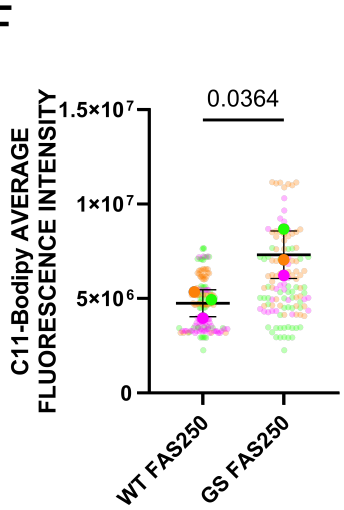
F
0.0364
C11-Bodipy AVERAGE FLUORESCENCE INTENSITY
WT FAS250
GS FAS250

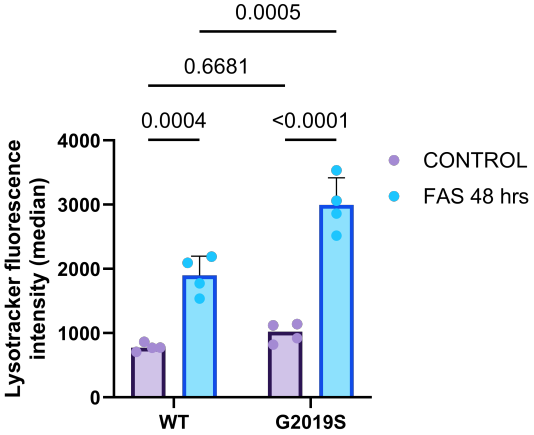
D
0.0005
0.6681
0.0004
<0.0001
Lysotracker fluorescence intensity (median)
CONTROL
FAS 48 hrs
WT
G2019S

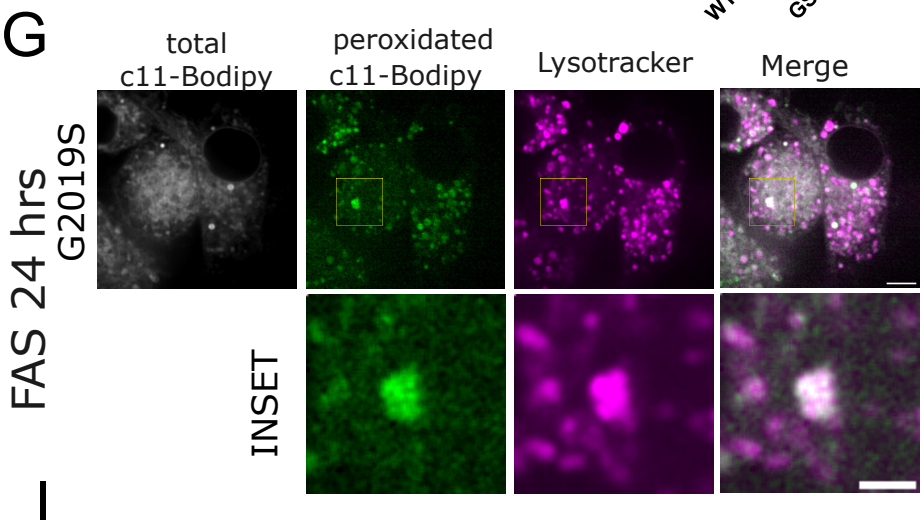
G
total c11-Bodipy
peroxidated c11-Bodipy
Lysotracker
Merge
FAS 24 hrs
G2019S
INSET

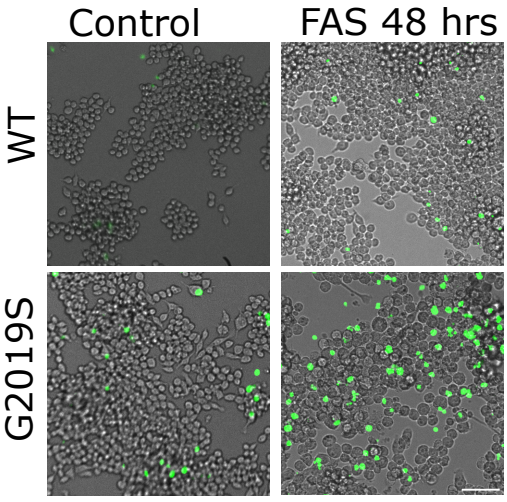
H
Control
FAS 48 hrs
WT
G2019S

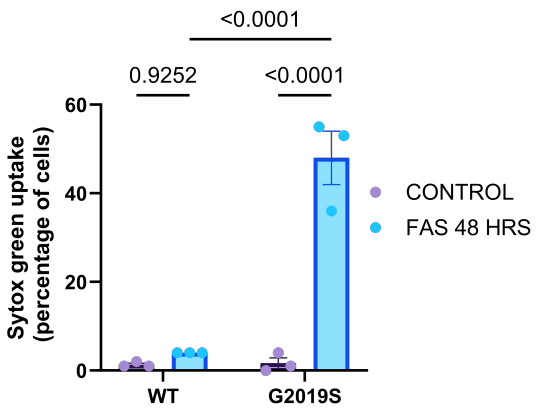
I
<0.0001
0.9252
<0.0001
Sytox green uptake (percentage of cells)
CONTROL
FAS 48 HRS
WT
G2019S
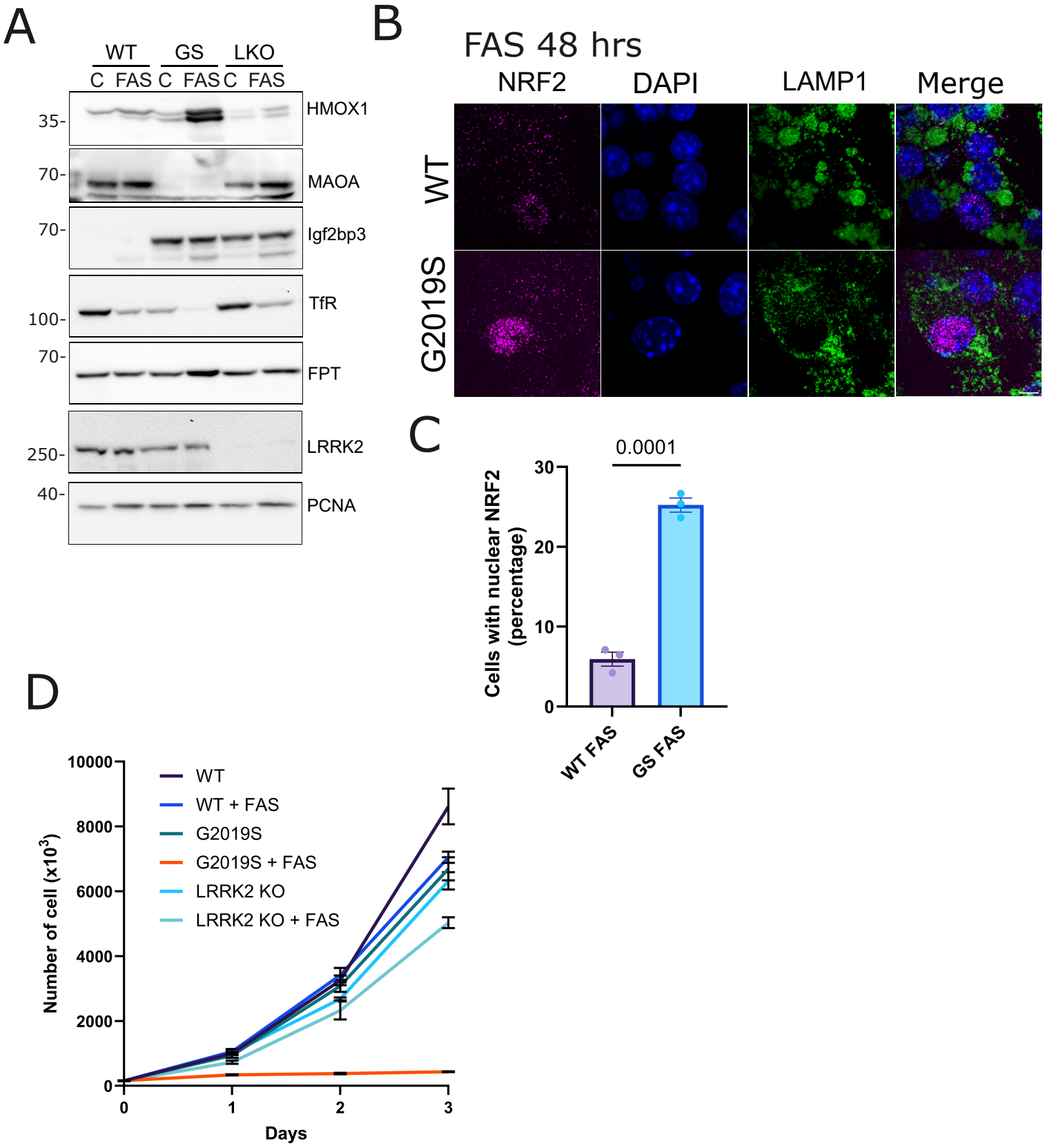
SUPPLEMENTARY FIGURE 4